PASJ: Publ. Astron. Soc. Japan **54**, 327–352, 2002 June 25

Study of the X-Ray Background Spectrum and Its Large-Scale Fluctuation with ASCA

Akihiro KUSHINO,[1] Yoshitaka ISHISAKI,[2] Umeyo MORITA,[2] Noriko Y. YAMASAKI,[2]
Manabu ISHIDA,[2] Takaya OHASHI,[2] and Yoshihiro UEDA[3]
[1]*National Space Development Agency of Japan (NASDA), 2-1-1 Sengen, Tsukuba, Ibaraki 305-8505*
kushino.akihiro@nasda.go.jp
[2]*Department of Physics, Tokyo Metropolitan University, 1-1 Minami-Osawa, Hachioji, Tokyo 192-0397*
[3]*The Institute of Space and Astronautical Science (ISAS), 3-1-1 Yoshinodai, Sagamihara, Kanagawa 229-8510*

(Received 2002 January 7; accepted 2002 April 9)

Abstract

We studied the energy spectrum and the large-scale fluctuation of the X-ray background with the *ASCA* GIS instrument based on the *ASCA* Medium Sensitivity Survey and Large Sky Survey observations. A total of 91 fields with Galactic latitude $|b| > 10^\circ$ were selected with a sky coverage of 50 deg^2 and 4.2 Ms of exposure. For each field, non-X-ray events were carefully subtracted and sources brighter than $\sim 2 \times 10^{-13}$ erg cm^{-2} s^{-1} (2–10 keV) were eliminated. Spectral fits with a single power-law model for the individual 0.7–10 keV spectra showed a significant excess below ~ 2 keV, which could be expressed by an additional thermal model with $kT \simeq 0.4$ keV or a steep power-law model with a photon index of $\Gamma^{\rm soft} \simeq 6$. The 0.5–2 keV intensities of the soft thermal component varied significantly from field to field by $1\sigma = 52^{+4}_{-5}\%$, and showed a maximum toward the Galactic Center. This component is considered to be entirely Galactic. As for the hard power-law component, an average photon index of 91 fields was obtained to be $\Gamma^{\rm hard} = 1.412 \pm 0.007 \pm 0.025$ and the average 2–10 keV intensity was calculated as $F_{\rm X}^{\rm hard} = (6.38 \pm 0.04 \pm 0.64) \times 10^{-8}$ erg cm^{-2} s^{-1} sr^{-1} (1σ statistical and systematic errors). The Galactic component is marginally detected in the hard band. The 2–10 keV intensities show a 1σ deviation of $6.49^{+0.56}_{-0.61}\%$, while deviation due to the reproducibility of the particle background is 3.2%. The observed deviation can be explained by the Poisson noise of the source count in the f.o.v. (~ 0.5 deg^2), even assuming a single $\log N - \log S$ relation on the whole sky. Based on the observed fluctuation and the absolute intensity, an acceptable region of the $\log N - \log S$ relation was derived, showing a consistent feature with the recent *Chandra* and *XMM-Newton* results. The fluctuation of the spectral index was also examined; it implied a large amount of hard sources and a substantial variation in the intrinsic source spectra ($\Gamma_{\rm S} \simeq 1.1 \pm 1.0$).

Key words: cosmology: diffuse radiation — galaxies: active — surveys — X-rays: diffuse background — X-rays: general

1. Introduction

The Cosmic X-ray Background, hereafter called CXB, dominates the hard X-ray surface brightness (Fabian, Barcons 1992), and was discovered with the Aerobee sounding rocket carrying three Geiger counters (Giacconi et al. 1962) along with the first extra-solar X-ray source, Sco X-1. The effort of resolving the CXB into discrete sources has produced a $\log N - \log S$ relation, which gives the number density (N) of discrete sources above a certain flux level (S). This study made a major advance recently with the advent of the *Chandra* X-ray Observatory. The detection limit of *Chandra* is down to $S \sim 10^{-16}$ erg cm^{-2} s^{-1} in the 2–10 keV band, and some of the sources are too faint for optical identifications to be made. In this energy range, more than half (60–90%) of the CXB emission has been resolved into discrete sources (e.g. Mushotzky et al. 2000 for the SSA13 field; Brandt et al. 2001 for the *Chandra* Deep Field North; Tozzi et al. 2001 for the *Chandra* Deep Field South). Moreover, recent *Chandra* and *XMM-Newton* results indicate a turn-over of around $S \sim 2 \times 10^{-14}$ erg cm^{-2} s^{-1} (Campana et al. 2001; Hasinger et al. 2001; Baldi et al. 2002). Above this flux level, the relation seems to be consistent with a uniform distribution of sources in Euclidean space, namely, $N(>S) \propto S^{-1.5}$ (Piccinotti et al. 1982; Hayashida et al. 1992; Ueda et al. 1999a,b). At the present time, the 2–10 keV CXB has been almost resolved into discrete sources, leaving at most 10–20% at the faintest flux limit. The main uncertainty of the resolved fraction lies in the measurement of the total intensity of the CXB, which requires a well-calibrated detector with a low internal background, as well as large sky coverage.

It also became clear that the emission consists of roughly two components. The hard-band emission in $\sim$ 2–10 keV shows almost an isotropic distribution in the sky, and the spectrum is characterized by a power-law spectrum with a photon index of $\Gamma \simeq 1.4$ (e.g. Marshall et al. 1980: 3–15 keV; Gendreau et al. 1995: 1–10 keV; Miyaji et al. 1998: 1–10 keV; Vecchi et al. 1999: 1–8 keV). The survey observations by *Uhuru* (2–7 keV) and *HEAO 1* A-2 ($\sim$ 2–10 keV) showed that the dipole amplitude after removing the Galactic contribution were $0.61 \pm 0.26\%$ (Protheroe et al. 1980) and $\sim 0.5\%$ (Shafer, Fabian 1983), respectively. Below ~ 2 keV, the spectrum becomes steeper with $\Gamma \simeq 2.1$ (e.g. Hasinger 1992 at ~ 1 keV). The *ROSAT* all-sky survey observation showed

significant structures in the soft X-ray background which are correlated mainly with the Galactic distribution of the hot gas (Snowden et al. 1995). As for the absolute intensity of the CXB, there is fairly large uncertainty among the measurements; namely, the reported intensities at 1 keV are 13.4 ± 0.3 (Hasinger 1992), 9.4 ± 0.4 (Gendreau et al. 1995) and $10.4^{+1.4}_{-1.1}$ (Parmar et al. 1999) photon $\mathrm{keV}^{-1}\,\mathrm{cm}^{-2}\,\mathrm{s}^{-1}\,\mathrm{sr}^{-1}$. Barcons et al. (2000) compiled previous measurements of the CXB intensity with the *ASCA*, *BeppoSAX*, and *ROSAT*, and pointed out that these differences are primarily caused by the cosmic variance, i.e. spatial variation of source count due to the limited solid angle of sky coverage, and in some part resulted from instrumental cross-calibration errors and subtraction process of the Galactic contribution.

X-ray surveys with optical follow-up observations (e.g. Schmidt et al. 1998; Akiyama et al. 2000; Ishisaki et al. 2001) have identified many active galactic nuclei (AGNs) and provided information about their spectral evolution. There is a significant discrepancy between the spectral indices of the CXB above ~ 2 keV ($\Gamma \simeq 1.4$) and of type-1 Seyfert galaxies ($\Gamma \simeq 1.7$), which led to a model that a significant fraction of AGN is heavily absorbed (Madau et al. 1994; Comastri et al. 1995; Gilli et al. 2001). In fact, for the sources with $S \gtrsim 10^{-15}\,\mathrm{erg\,cm^{-2}\,s^{-1}}$, the *XMM-Newton* satellite revealed that around half of them are strongly absorbed in their spectra (Hasinger et al. 2001). In the flux range $S \sim 10^{-14}$–$10^{-11}\,\mathrm{erg\,cm^{-2}\,s^{-1}}$, a spectral survey from *ASCA* showed that the average spectral slope becomes progressively harder as the sources become fainter, and the observed photon index of 2.1 at around $10^{-11}\,\mathrm{erg\,cm^{-2}\,s^{-1}}$ turns to 1.6 at around $10^{-13}\,\mathrm{erg\,cm^{-2}\,s^{-1}}$ in the 0.7–10 keV band (Ueda et al. 1999b). A precise determination of the spectral shape of the CXB and an investigation of its field-to-field difference would provide rich information to understand the spectral evolution of AGNs taking place around the flux of $10^{-13}\,\mathrm{erg\,cm^{-2}\,s^{-1}}$.

The *ASCA* Medium-Sensitivity Survey (AMSS) is a serendipitous survey, consisting of 368 fields which can be regarded as a random sampling of the CXB. Ueda et al. (2001) produced a catalog of 1343 X-ray sources based on the AMSS, and gave a fairly tight $\log N - \log S$ relation in the flux range above $7 \times 10^{-14}\,\mathrm{erg\,cm^{-2}\,s^{-1}}$ (Ueda et al. 1999b). Also, combined with the *ASCA* Large Sky Survey (Ueda et al. 1998, 1999a), the main aim of the present study is to determine the absolute intensity and the spectral shape of the CXB as precisely as possible. The data after the point-source elimination formed the basis for the present study. It would also enable us to constrain the $\log N - \log S$ relation or the intrinsic spectral distribution of the constituent sources through the fluctuation analysis, as well as to look into the large-scale distribution of the CXB. The GIS system (Ohashi et al. 1996; Makishima et al. 1996) consists of two gas imaging spectrometers, which have well-studied and low internal background, simultaneously providing a large ($\gtrsim 40'$ in diameter) field of view (f.o.v.), when compared with the *XMM-Newton* PN and MOS CCDs and *Chandra* ACIS CCDs. These properties are powerful for studying the spectral features of the CXB.

The remainder of this paper is organized as follows. In section 2, we discuss the selection criteria of the fields employed in the present paper for the CXB analysis and explain how energy spectra are extracted. In section 3, we present the fitting results. In section 4, the large-scale distributions in the spectral parameters are investigated. In section 5, using simulations which take into account the complicated response of *ASCA*, we evaluate the CXB intensity and constrain the $\log N - \log S$ relation and the spectral distribution of sources from the observed fluctuation. In section 6, we discuss implications of the results, and the summary will be given in section 7.

2. Observation and Analysis

The present study was carried out with a GIS instrument consisting of GIS 2 and GIS 3 sensors (Ohashi et al. 1996; Makishima et al. 1996). The detectors had a wide ($\sim 40'$ in diameter) f.o.v. and a moderate spatial resolution of $\sim 3'$ (Half Power Diameter) combined with the X-Ray Telescope (XRT; Serlemitsos et al. 1995). Our primary goal of the analysis was to determine the parameters of the CXB for each direction which cannot be resolved into discrete sources with the GIS, namely, the *unresolved* CXB. Due to the low surface brightness of the unresolved CXB, we had to take into account several issues that would not matter very much in point-source studies. First of all, the sample fields must be carefully selected in order to obtain reasonable constraints on the parameters. The second one is to minimize and precisely estimate the amount of fake signals caused mainly by charged particles, which we call the Non-X-ray Background (NXB). The third one is to eliminate *resolved* sources in the GIS f.o.v. The last one is the instrumental response for the unresolved CXB.

2.1. Selection of the Fields

Our sample fields were primarily selected from the first AMSS fields (Ueda et al. 2001), which consisted of 368 combined fields observed between 1993 May and 1996 December with the Galactic latitude $|b| > 10^\circ$. We also included the field of the *ASCA* Large Sky Survey (LSS; Ueda et al. 1998, 1999a), dividing the LSS field into four, labeling them a-LSS, b-LSS, c-LSS, and d-LSS, from south-west to north-east.

In our prompt sample, several fields were composed of multiple pointing observations, covering a larger sky area than that of a single pointing. Furthermore, most of the AMSS fields were pointed to certain targets and often contained rather bright X-ray sources to study the CXB. Since the Point Spread Function (PSF) of the XRT has long outskirt, approximated by

$$\mathrm{PSF}(r) = \exp\left(-\frac{r}{1'.02}\right) + 0.0094\exp\left(-\frac{r}{6'.14}\right), \qquad (1)$$

a bright target source would contaminate the whole detector area ($r \lesssim 20'$). We therefore selected fields based on the following criteria:

1. Total exposure time summed up over all pointings is longer than ~ 20 ks.
2. No known extended X-ray sources is present in the field, e.g., nearby galaxies, star-forming regions, or supernova remnants.
3. The mean count rate including the NXB is lower than $0.3\,\mathrm{count\,s^{-1}}$ per one GIS sensor in 0.7–10 keV, accumulated within a radius of 22 mm ($\simeq 22'$) from the optical

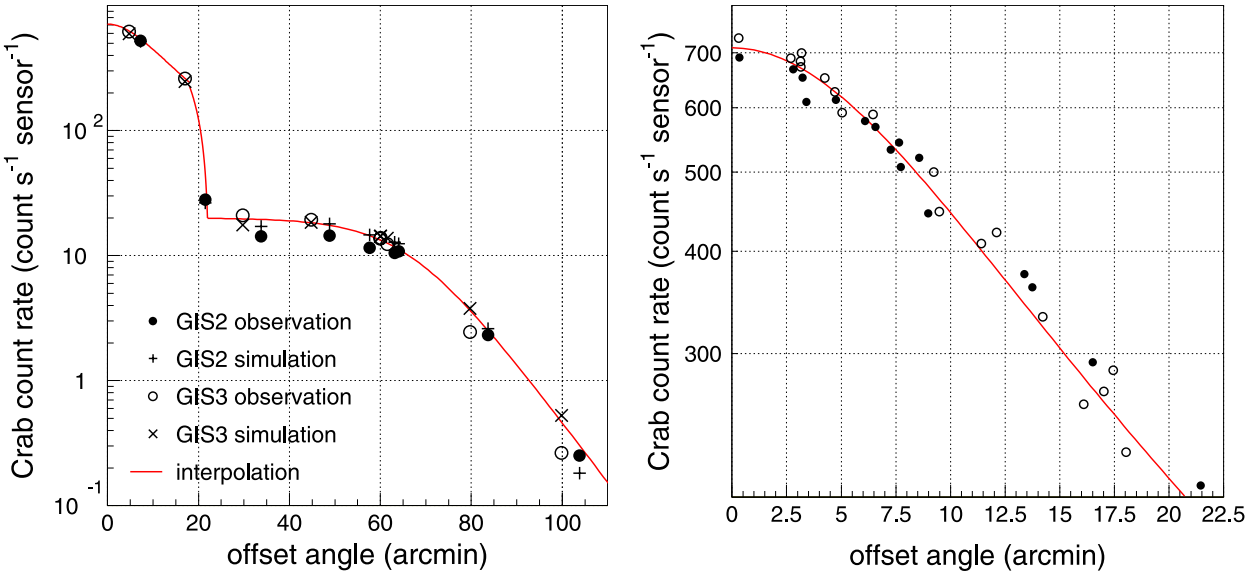

Fig. 1. 0.7–10 keV count rate of the Crab nebula observed with GIS at various offset angles from the optical axis of each GIS sensor. Events within a radius of 20 mm ($\simeq 20'$) were accumulated, and the CXB and the NXB counts were subtracted after being corrected for the dead time. The left panel is shown for a wide range of offset angles of up to ~ 100 arcmin. The observed count rates for each sensor are plotted in circles, as well as the expectations from the simulation plotted in crosses. The solid line represents an interpolated function using analytical formulae. The right hand panel is a close-up, when the Crab nebula is placed inside the GIS f.o.v.

axis of each sensor. For multi-pointing observations, we accept fields when at least one pointing fulfills this condition.

4. The remained sky area after the source elimination ("Area 2" column of table 1) is more than two thirds of the original sky area ("Area 1").

Exactly 100 fields satisfied these conditions.

Since the XRT allows some fraction of photons from outside of the f.o.v. to pass through (stray light; Tsusaka et al. 1995), it is a significant problem in the CXB study with *ASCA*. Figure 1 represents the 0.7–10 keV count rate of the Crab nebula pointed at various offset angles from the optical axis of each GIS sensor. When the Crab nebula was placed at $\sim 1^\circ$ away from the optical axis, namely far outside of the GIS f.o.v., its count rate was still larger than 10 count s^{-1} sensor^{-1} in 0.7–10 keV. Since the CXB gave only ~ 0.12 count s^{-1} sensor^{-1} in the same energy band, the stray flux needed to be carefully examined. In order to avoid any influence of the stray light in the present analysis, we further selected those fields which had no bright sources around the f.o.v. We mainly consulted with the *ROSAT* All-Sky Survey Bright Source Catalog (RASS-BSC; Voges et al. 1999), which lists sources with a flux limit of 2.8×10^{-13} erg cm^{-2} s^{-1}, assuming a power-law photon index of $\Gamma = 2$ in the 0.1–2.4 keV energy band. However, the sensitive energy range of *ROSAT* is limited to below ~ 2 keV and sources with hard spectra or strong absorption would be missed. The *HEAO 1* A-1 X-ray source catalog (Wood et al. 1984) was also used to follow up such cases. *HEAO 1* A-1 is sensitive above ~ 2 keV, and the flux limit is 4.78×10^{-12} erg cm^{-2} s^{-1} in 2–10 keV for a Crab-like spectrum.

Based on these catalogs, the distance distribution of the cataloged sources from the centers of the selected 100 fields was determined as shown in figure 2. In this figure, the source intensities are plotted as a function of the offset angle. The solid curve indicates a level where sources above it could contribute to the CXB intensity accumulated within the whole GIS f.o.v. ($r < 20$ mm $\simeq 20'$) by more than 2.5%. This estimation is based on a calibration observation of the Crab nebula at various offset angles, which is indicated in figure 1 by the solid line. Using the *ROSAT* sources, we excluded 9 fields in which there were sources above the 2.5% line *outside* the GIS f.o.v. ($r > 20$ mm $\simeq 20'$). We did not exclude fields if bright sources are *inside* the f.o.v., i.e. in the hatched region in figure 2, since they would be eliminated in the source-elimination process (see subsection 2.3). As for the *HEAO 1* sources, any fields were excluded if sources brighter than 1.0×10^{-10} erg cm^{-2} s^{-1} were present within $r < 4^\circ$. This is because the positional errors of the *HEAO 1* sources are quite large ($\sim 1^\circ$). One field was picked up by the *HEAO 1*-source selection; however, it had already been marked by the *ROSAT*-source selection. We therefore excluded 9 fields in total. One of the LSS fields (a-LSS) was rejected here.

After these field selections, we ended up with 91 fields whose sky distribution is shown in figure 3 together with the original AMSS and LSS fields. The names and coordinates of the fields are listed in table 1. Among them, 33 fields consist of multi-pointing observations. The exposure time of the 91 (88) fields amounts to 4240.54 (3844.27) ks and the covering sky area extends 49.53 (42.77) deg^2, where the numbers in parentheses denote those without the three LSS fields. According to the AMSS and the LSS catalogs, the brightest source in the 91 fields is 1AXGJ 085449+2006 with 0.7–7 keV flux of 5.89×10^{-12} erg cm^{-2} s^{-1} in OJ 287 field, or 1AXG J004847+3157 with 2–10 keV flux of 7.58×10^{-12} erg cm^{-2} s^{-1} in Mrk 348 field, depending on the chosen energy band. Both sources

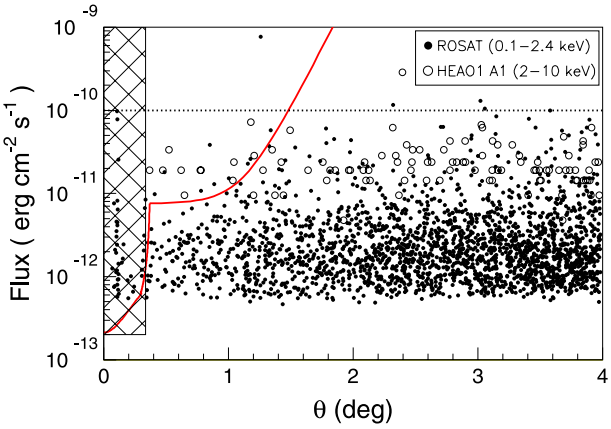

Fig. 2. Fluxes of cataloged bright sources within 4° from the center of 100 pointed fields. The filled and open circles correspond to the sources in the RASS-BSC (Voges et al. 1999) and in the *HEAO 1* A-1 X-ray source catalog (Wood et al. 1984), respectively. The dotted line is used to discriminate the *HEAO 1* sources which have large position errors, and the solid curve is for the *ROSAT* sources. Sources lying above these lines and outside of the GIS field (hatched region) can affect the measured CXB flux by more than 2.5%; and the relevant fields were discarded from the analysis.

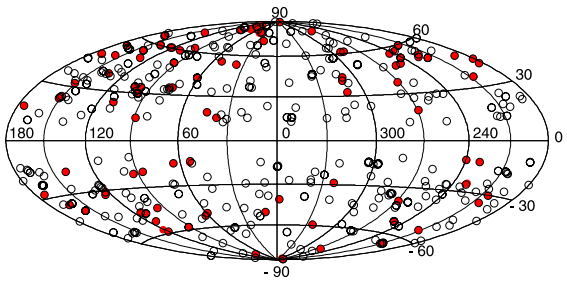

Fig. 3. Distribution of the 91 analyzed fields, shown with filled circles, in the Galactic coordinate. The open circles are other AMSS and LSS fields. The plotted symbols do not indicate the actual size of the observed field.

correspond to the target, itself, i.e. OJ 287 or Mrk 348. Among the 88 AMSS fields, there are 184 (141) sources with their 0.7–7 (2–10) keV flux brighter than 2×10^{-13} erg cm^{-2} s^{-1} in each energy band in the AMSS catalog.

2.2. *Data Screening and NXB Subtraction*

We screened all of the GIS events detected in each sample field, first employing the standard event selection criteria: (1) the GIS should be in the nominal observation mode, i.e. the PH normal mode with the nominal bit assignment, the spread discriminator turned on, and the satellite not in the South Atlantic Anomaly (SAA) where the high-voltage supply of the GIS is switched off; (2) the elevation of f.o.v. should be $\geq 5°$ (or 25°) above the night (or sunlit) Earth rim; (3) the geomagnetic cutoff rigidity (COR) should be $\gtrsim 6$ GV. We performed further event screening utilizing the GIS monitor counts (H0 + H2; see Ohashi et al. 1996; Makishima et al. 1996), Radiation Belt Monitor (RBM) count, and COR. This additional selection improved the reproducibility of the NXB estimation, mainly by rejecting data affected by sporadic increases in the NXB count, which were due probably to the concentration of charged particles on the satellite orbit. A stricter condition for the RBM count was applied around the SAA and Hawaii. Details of the screening procedure are described in Ishisaki (1996) and Ishisaki et al. (1997).

The obtained event list contains not only the CXB photons, but also the NXB events, which must be carefully subtracted. The corresponding spectra or images of the NXB were separately created, using observations when the XRT was pointed to the night Earth. Under the same condition as described in the previous paragraph, we processed seven years of night-Earth data from 1993 June to 2000 May, with a net exposure time of 4880.43 ks. We further sorted both the observed data and the night-Earth data into six intervals of the H0 + H2 monitor count in 5 count s^{-1} steps, and performed NXB subtraction for each interval. This is because the H0 + H2 monitor count, which is tightly correlated with the NXB count (Makishima et al. 1996), can be used as a good NXB indicator during on-source observations.

There is also a long-term change of the NXB count rate, which is shown in figure 4. The count rate gradually increased for the first four years, and then turned to decreasing, peaking at around 1997–1998. This long-term change was presumably caused by a gradual drop in the satellite altitude and the cycle of the solar activities with a period of ~ 11 yr. During the quiescent state of the solar activities, which is at the minimum around 1996–1997, the atmosphere shrunk so that the density of charged particles increased. Since the observation date of our sample fields ranged from 1993 June to 1996 December, there could be about a $\pm 10\%$ error in the NXB estimation unless the long-term trend were corrected. We fitted the trend by a fourth-order polynomial, which was used for the correction.

We estimated that the NXB had been reproduced by an accuracy of 3% using the H0 + H2 monitor count and corrected for the long-term trend. Therefore, the systematic uncertainty in the NXB subtraction affects the CXB intensity by at most 10%, even at ~ 7 keV where the NXB dominates the CXB (see figure 7).

2.3. *Source Elimination*

The CXB intensity can be defined by equation (6) in subsection 5.1, even including the contribution from very bright sources, namely, by setting $S \rightarrow \infty$ in equation (6) in subsection 5.1. On the other hand, because actual observations are usually biased to the faint so-called blank sky, the observed intensity needs a certain correction. This correction depends on the observed flux range, $S < S_0$, where it is assured that only the sources with their fluxes fainter than S_0 exist in a sample field. Therefore, it is essentially required to eliminate *resolved* sources on the source flux basis. We employed a certain fixed value of $S_0 \simeq 2.0 \times 10^{-13}$ erg cm^{-2} s^{-1} (2–10 keV), and defined that sources brighter than S_0 were *resolved* and that the remained X-ray emission was the *unresolved* CXB. This procedure is also important in order to overcome the selection bias of the AMSS fields, because they are originally intended to observe specific targets. Since the AMSS and the LSS catalogs are constructed on the source significance basis, some sources with low significances but possible high flux or

Table 1. Field list.

Field ID*	Field name†	Number of pointing (s)	Observation date‡	N_H§ (10^{20} cm^{-2})	$l^{\|\|}$ (deg)	$b^{\|\|}$ (deg)	Exposure (ks)	Area 1♯ (deg^2)	Area 2** (deg^2)
—	LSS	76	1993/12/26	1.1	75.35	83.21	515.4	7.19	5.98
1	b-LSS	21	1994/01/05	1.1	73.86	83.85	130.2	2.32	1.86
2	c-LSS	20	1994/06/17	1.1	77.74	82.61	138.7	2.26	1.87
3	d-LSS	18	1995/01/07	1.1	80.38	81.40	127.4	2.18	1.58
4	DRACO	3	1993/06/04	4.2	102.28	33.92	57.0	0.70	0.66
5	JUPITER	1	1993/06/06	2.2	286.22	61.22	20.4	0.40	0.32
6	NEP FIELD	8	1993/06/09	4.2	96.38	29.90	118.5	0.58	0.47
7	QSF 3	4	1993/07/11	1.6	250.83	−51.99	60.2	0.43	0.37
8	ARP 220	1	1993/07/26	4.3	36.48	53.13	23.1	0.40	0.39
9	3C 368	1	1993/09/12	9.1	37.57	15.27	19.9	0.40	0.36
10	IRAS F10214+4724	3	1993/11/04	1.2	168.04	55.07	88.7	0.56	0.55
11	IRAS 09104	1	1993/11/12	1.0	180.98	43.66	34.5	0.40	0.27
12	MNVTEST	2	1993/11/29	1.8	323.86	−59.29	38.2	0.47	0.46
13	SN 1986J	2	1994/01/21	7.5	140.37	−17.53	81.3	0.41	0.28
14	AO 0235+164	5	1994/02/04	9.0	156.79	−39.22	42.4	0.41	0.29
15	NGC 1614	1	1994/02/16	6.1	204.53	−34.47	28.0	0.40	0.29
16	NGC 1667	1	1994/03/06	5.5	204.13	−30.21	31.0	0.40	0.33
17	4C 41.17	1	1994/03/23	10.4	174.71	17.39	24.2	0.40	0.28
18	NGC 3690	2	1994/04/16	0.9	141.89	55.38	30.5	0.54	0.46
19	K416	1	1994/05/22	1.8	97.07	62.49	24.4	0.40	0.35
20	NGC 4449	1	1994/05/25	1.4	137.20	72.38	37.8	0.40	0.33
21	PHL 5200	2	1994/06/21	5.2	59.13	−49.59	92.7	0.54	0.37
22	NGC 4418	1	1994/06/11	2.1	289.87	61.31	26.8	0.40	0.34
23	GSGP 4	4	1994/06/24	1.9	260.39	−88.46	110.5	1.37	1.21
24	DI PEG	1	1994/06/25	4.0	96.11	−43.64	24.3	0.40	0.31
25	PG 1404+226	1	1994/07/13	2.1	21.30	72.42	27.6	0.40	0.28
26	IRAS 15307+325	1	1994/07/22	2.0	51.95	54.92	30.1	0.40	0.39
27	Z SYSTEM	5	1994/08/09	2.2	209.43	−65.08	109.9	1.67	1.41
28	MG 2016+112	2	1994/10/24	15.5	53.88	−14.04	94.4	0.79	0.69
29	IRAS 20460+192	1	1994/10/27	11.2	64.55	−14.86	32.5	0.40	0.31
30	BLANK SKY	1	1994/11/10	13.4	89.02	14.51	23.6	0.40	0.35
31	EPSILON CMA	1	1994/11/16	14.8	239.85	−11.22	34.4	0.40	0.31
32	OJ 287	3	1994/11/18	3.0	206.80	35.86	88.5	0.55	0.41
33	RASS 1011+1736	1	1994/11/30	3.2	219.56	52.58	31.8	0.40	0.39
34	XY LEO	2	1994/12/02	3.3	217.77	49.85	19.0	0.40	0.31
35	Mrk 231	3	1994/12/05	1.3	122.03	60.27	117.1	0.83	0.73
36	NGC 7320	1	1994/12/07	7.9	93.18	−21.08	28.6	0.40	0.30
37	CN LEO	1	1994/12/16	2.9	244.08	56.23	44.7	0.40	0.30
38	Mrk 273	1	1994/12/27	1.1	107.95	59.61	29.8	0.40	0.30
39	NGC 5135	1	1995/01/22	4.6	311.87	32.50	35.6	0.40	0.28
40	Q1508+5714	2	1995/03/02	1.5	93.25	51.25	63.4	0.48	0.37
41	GB 930704	3	1995/03/17	5.2	151.34	23.89	25.0	1.18	0.84
42	NGC 4125	1	1995/04/05	1.8	130.21	51.27	24.8	0.40	0.30
43	TXFS 1011+144	1	1995/05/18	3.9	224.35	51.22	28.1	0.40	0.37
44	MS 1054.5−0321	1	1995/05/23	3.6	256.54	48.56	48.6	0.40	0.31
45	CL 2236−04	1	1995/05/31	4.0	63.00	−51.22	25.0	0.40	0.35
46	PG 1247+267	1	1995/06/17	0.9	273.35	89.22	26.1	0.40	0.32
47	NGC 4450	1	1995/06/20	2.4	273.70	78.54	25.6	0.40	0.33
48	QSO CLUSTER	3	1995/07/03	1.1	40.01	79.08	114.8	1.19	0.93
49	NGC 5084	1	1995/07/08	8.2	311.61	40.51	25.1	0.40	0.32
50	SA 68	2	1995/07/09	4.2	111.10	−46.22	47.2	0.59	0.56
51	Mrk 348	1	1995/08/04	5.8	122.28	−30.80	32.2	0.40	0.28
52	NGC 1332	1	1995/08/05	2.2	212.03	−54.30	44.4	0.40	0.36
53	PKS 0634−205	1	1995/10/09	22.3	229.89	−12.29	25.9	0.40	0.32

Table 1. (Continued)

Field ID*	Field name†	Number of pointing (s)	Observation date‡	N_H§ (10^{20} cm^{-2})	l‖ (deg)	b‖ (deg)	Exposure (ks)	Area 1♯ (deg^2)	Area 2** (deg^2)
54	IRAS 20551−425	1	1995/10/19	3.9	358.50	−40.77	25.6	0.40	0.30
55	HS 1946+7658	1	1995/10/21	7.6	109.12	23.52	29.7	0.40	0.40
56	RGH 12	1	1995/10/29	1.5	190.96	47.33	34.9	0.40	0.34
57	UKMS 1	1	1995/11/12	0.8	156.69	49.55	41.0	0.40	0.32
58	F568−06	2	1995/11/16	2.0	217.50	59.50	38.8	0.40	0.29
59	NGC 7217	1	1995/11/19	10.5	86.40	−19.76	62.0	0.40	0.27
60	NGC 1672	1	1995/11/23	2.3	268.82	−38.88	27.3	0.40	0.27
61	BJS 855	1	1995/11/27	4.0	250.20	49.31	32.2	0.40	0.35
62	PG 1148+549	1	1995/12/07	1.2	140.39	60.39	27.4	0.40	0.31
63	IRAS 00317−2142	1	1995/12/11	1.6	86.77	−83.16	27.8	0.40	0.30
64	NGC 5005	1	1995/12/13	1.1	101.12	79.18	27.1	0.40	0.27
65	NGC 5018	1	1996/01/16	7.0	310.05	43.07	28.9	0.40	0.37
66	4C 38.41	4	1996/03/04	1.0	61.22	42.31	26.9	0.44	0.34
67	AR UMa	1	1996/04/27	1.8	167.63	64.89	40.0	0.40	0.36
68	PG 1114+445	1	1996/05/05	1.8	164.87	64.43	49.2	0.40	0.30
69	HE 1104−1805	1	1996/05/31	4.6	270.78	37.79	30.8	0.40	0.28
70	RX J1716.6+670	2	1996/06/09	3.7	97.63	34.05	54.7	0.40	0.31
71	B2 1308+326	2	1996/06/10	1.1	86.16	83.41	28.0	0.40	0.28
72	Q2345+007	2	1996/06/26	3.8	92.15	−58.00	54.4	0.40	0.34
73	IRAS 00235+102	1	1996/07/07	5.1	112.92	−51.58	31.6	0.40	0.35
74	NGC 612	1	1996/07/12	1.8	261.19	−77.05	58.8	0.40	0.35
75	CL 0024+17	1	1996/07/21	4.2	114.54	−45.20	34.6	0.40	0.29
76	NGC 315	1	1996/08/05	5.9	124.57	−32.39	26.6	0.40	0.33
77	MS 0302.7+1658	4	1996/08/18	10.9	162.86	−34.89	98.7	0.67	0.47
78	V 471 TAURI	1	1996/08/26	15.8	172.44	−27.83	36.3	0.40	0.28
79	RX J1802+1804	1	1996/09/30	8.5	44.00	18.82	50.0	0.40	0.35
80	A548	2	1996/10/10	1.9	229.79	−25.21	62.4	0.79	0.59
81	IRAS 19254−7245	1	1996/10/16	6.0	322.40	−28.70	24.8	0.40	0.33
82	IRAS 07598+6508	1	1996/10/29	4.3	151.10	32.14	31.5	0.40	0.31
83	HERC-1	2	1996/11/02	2.4	75.56	34.83	45.0	0.79	0.59
84	IRAS 08572+3915	1	1996/11/03	2.6	183.33	41.10	22.7	0.40	0.31
85	A851	3	1996/11/16	1.2	171.64	48.27	81.7	0.56	0.48
86	NGC 7130	1	1996/11/18	2.0	9.78	−50.32	26.0	0.40	0.35
87	10303+7401	1	1996/11/26	4.1	134.66	40.06	32.2	0.40	0.36
88	4C 06.41	2	1996/12/13	2.8	241.14	52.76	67.8	0.40	0.28
89	M96	1	1996/12/16	2.8	234.51	57.15	30.8	0.40	0.39
90	IC 2560	1	1996/12/19	6.5	269.48	19.12	27.2	0.40	0.37
91	PG 0043+039	2	1996/12/21	3.3	121.04	−58.05	51.1	0.80	0.75

* Field identification number defined in this paper.
† Corresponding to the target name in the AMSS (Ueda et al. 2001) except for the LSS fields (Ueda et al. 1998).
‡ For multi-pointing fields, the earliest observation date is listed.
§ Galactic hydrogen column density toward to the observed field estimated from Dickey and Lockman (1990).
‖ Center of f.o.v. in the Galactic coordinates.
♯ Area before the source elimination.
** Area after the source elimination.

extended emission could be missed. We therefore developed an original method for eliminating sources by slightly modifying the source detection procedure of the AMSS. Throughout this paper, we call this method as "source elimination", which is described in the following paragraphs.

The resolved sources were eliminated using the observed data, itself, in each field. We first constructed a mosaic flat-field image $M^{\rm FLAT}$ in the sky coordinates. This is a probability map that is proportional to the intensity of resolved sources, after subtracting the NXB and the unresolved CXB, and correcting for the telescope vignetting and the exposure of each pointing. This image is useful to set a threshold in terms of the X-ray flux. The $M^{\rm FLAT}$ was created in the 0.7–7 keV band since the NXB is dominant in the higher energy band. In order to eliminate sources at the rim region effectively, events within a radius of 22 mm ($\simeq 22'$) from the optical axis of each GIS sensor were accumulated, which is by 10% larger than the radius of 20 mm ($\simeq 20'$) when we created an energy spectrum. A single $M^{\rm FLAT}$ image was created for each sample field, by summing up all pointings for both GIS 2 and GIS 3 in the

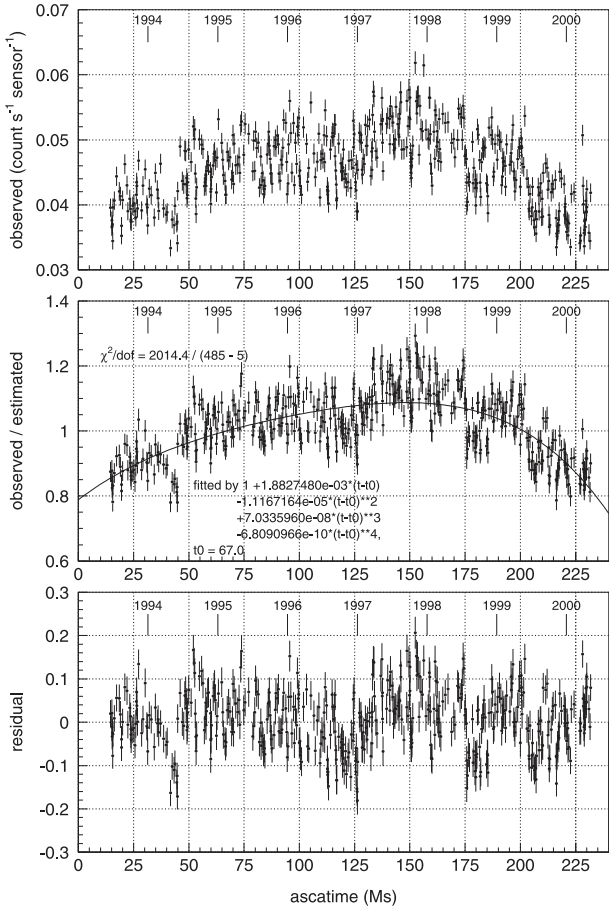

Fig. 4. Top panel: Long-term change of the observed NXB count rate (count s^{-1} $sensor^{-1}$) in the 0.7–7 keV band accumulated within 20 mm ($\simeq 20'$) from the optical axis of each GIS sensor. Each data point was determined from every 10 ks exposure of the night Earth between 1993 June and 2000 May, and plotted as a function of the mean *ASCA* time, which is defined as the elapsed time in second since 1993 January 1. Middle panel: Observed NXB count rate divided by the estimated one using the H0 + H2 monitor count. The long-term trend is fitted by the fourth order polynomial, which is indicated by the solid line. Bottom panel: Residuals of the fitting.

common sky coordinates.

The NXB image to be subtracted was generated for each pointing and for each sensor, as described in subsection 2.2. With regard to the unresolved CXB image, we created a template image for each GIS sensor, which was commonly used for every field and every pointing. This template was made from a sunlit-Earth image in 1–3 keV integrated over two years from 1993 June to 1995 June, because of its uniformness and extreme brightness. Since its spectrum is much softer than the CXB, we corrected the radial brightness profile for the XRT vignetting utilizing a radial profile of the superposed LSS image in 0.7–7 keV, in which irregularities due to the discrete sources are sufficiently smeared out. The normalization of the template was determined to give 88% intensity of the LSS field. Although this is an empirical factor, it is considered to be close to the unresolved fraction of the X-ray emission in the LSS field. Details are described by Ishisaki (1996).

After subtracting these two images, the observed image was

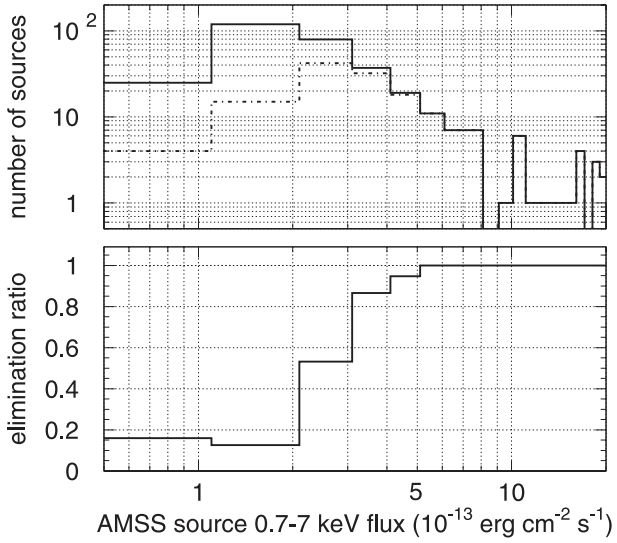

Fig. 5. Distribution of the 331 AMSS sources in our analyzed fields as a function of the 0.7–7 keV flux. In the top panel, the solid line shows all of the AMSS sources in the 91 fields, and the dash-dotted line indicates the masked-out ones in the source elimination. The bottom panel shows the elimination ratio for the AMSS sources.

cross-correlated with the PSF of the XRT + GIS system. Since the shape of the PSF of the XRT strongly depends on the source position on the detector, we calculated it by interpolating the Cyg X-1 images, which were observed with various offset angles and azimuth angles within a radius of $17'$ from the optical axis (Takahashi et al. 1995; Ikebe et al. 1997). The vignetting of the XRT was also corrected here. This series of processes was made for each sensor (2 sensors) and each pointing ($N_{\rm P}$ pointings), and afterwards all $2 \times N_{\rm P}$ images were summed up to build a single mosaic image. Finally, corrected for the exposure time considering the overlap of multiple pointings, the $M^{\rm FLAT}$ image was complete.

For the thus-obtained $M^{\rm FLAT}$ image, we settled on a certain threshold level which corresponded to $\sim 2 \times 10^{-13}\,{\rm erg\,cm^{-2}\,s^{-1}}$ (0.7–7 keV), and searched for peaks above it. This flux level was chosen because the sources were detected at a 5–10σ significance, depending on the distance from the optical axis, for a typical exposure of 30–40 ks. If we assumed a power-law spectrum of $\Gamma \simeq 1.7$, which is typical for the resolved sources, the threshold flux did not change very much (less than 10%) by altering the energy range from 0.7–7 keV into 2–10 keV. When a peak was detected, a circular region was masked out from the data. The radius of the mask was determined so that the remaining surface brightness due to the tail of the PSF would become less than 10% of the unresolved CXB. This calculation was conducted using equation (1), and the typical mask diameters were $9'$ and $14'$ for fluxes of $2 \times 10^{-13}\,{\rm erg\,cm^{-2}\,s^{-1}}$ and $1 \times 10^{-12}\,{\rm erg\,cm^{-2}\,s^{-1}}$, respectively. By omitting the masked sky regions, we created an energy spectrum for the remained area by accumulating events in each field. Since the outermost region of the GIS f.o.v. is dominated by the NXB, we collected events within a radius of 20 mm ($\simeq 20'$) from the optical axis of each sensor.

There are 331 sources listed in the AMSS catalog in our 88

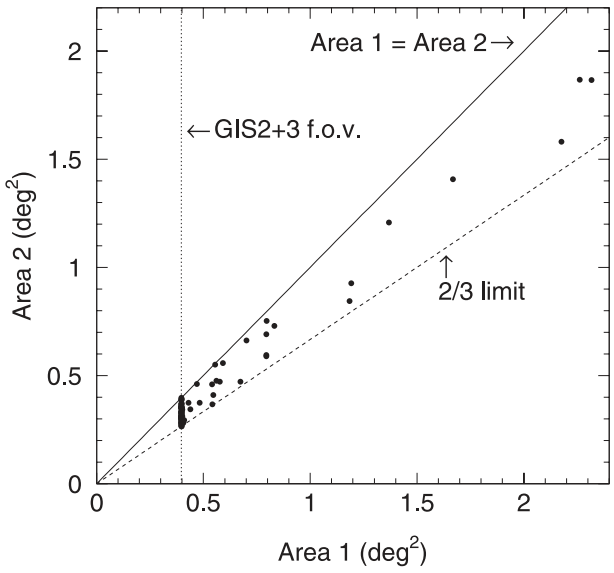

Fig. 6. Comparison of the sky coverage before and after the source elimination. The horizontal and vertical axes correspond to the area before (Area 1) and after (Area 2) the source elimination, respectively. Three lines which limit the data scattering are also indicated.

selected AMSS fields. As shown in figure 5, 90% of those AMSS sources were eliminated in this process at a flux level of 4×10^{-13} erg cm^{-2} s^{-1} in 0.7–7 keV. Some fraction of sources fainter than the threshold of $\sim 2 \times 10^{-13}$ erg cm^{-2} s^{-1} (0.7–7 keV) are also eliminated because they happen to exist neighboring other bright sources. For each field, the resultant sky area after the source elimination is compared with the original value in figure 6. The sky coverage was thus reduced by about 20% with this process.

2.4. *Instrumental Response*

An accurate instrumental (XRT + GIS) response is required to quantify the CXB spectrum. However the XRT response depends significantly on the off-axis angle, making the overall response to the CXB much different from that to a point source. The superposition of point-source responses within the integration region is still insufficient due to the stray light. Moreover, the responses are slightly different among the 91 sample fields, since the masking patterns of the source elimination are different from field to field.

In order to include these conditions in the response, we performed ray-tracing simulations for all 91 fields using the SimARF code (Ishisaki 1996; Honda et al. 1996; Shibata et al. 2001), which calculates the photon detection efficiency of the XRT + GIS system at each energy, and generates a so-called Auxiliary Response File (ARF). In those simulations, we assumed a flat surface brightness, which extends far beyond the GIS f.o.v., to be concrete up to 2.°5 from the optical axis of each sensor. This assumption is good enough as a first approximation, at least for the unresolved CXB after the source elimination. However, it leaves some room for considering that we can eliminate the resolved sources in the f.o.v., while we cannot do so for sources outside the f.o.v., from which some fraction of photons appear as the stray light. We deal with this effect in subsection 5.4.

Though a nuisance, the stray light was reproduced sufficiently well by a ray-tracing code (Tsusaka et al. 1995), which we calibrated against large offset observations of the Crab nebula up to $\sim 100'$, as shown in figure 1. The major origin of the stray light was due to the X-rays to come through abnormal paths, e.g. only one reflection by the primary mirror or via reflection off the mirror backside, which were fully taken into account in a ray-tracing simulation. The stray-light estimation is considered to be accurate to within $\pm 10\%$ of the CXB intensity, with only a mild energy dependence. We have confirmed that the SimARF generates an identical ARF for a point source in the f.o.v. with that made by ascaarf v2.81 in combination with the standard calibration database files, namely, `gis2/3_ano_on_flf_180295.fits` (telescope definition file), `xrt_ea_v2_0.fits` (effective area file), and `xrt_psf_v2_0.fits` (PSF file).

A so-called *ARF filter* was also applied to our SimARF ARF, which normalized the observed flux of the Crab nebula with XRT + GIS to the previously reported level and suppressed small residual structures in the spectral fitting. With the ARF filter, the Crab spectrum can be expressed by an absorbed power-law model with Galactic absorption of $N_{\rm H} = 2.90 \times 10^{21}$ cm^{-2}, a photon index of $\Gamma = 2.09$, and 2–10 keV flux of 2.16×10^{-8} erg cm^{-2} s^{-1} (absorption not corrected). The ARF filter was applied by default for the ascaarf ARF with the "arffil" parameter; the details are described in Fukazawa et al. (1997). As for the energy redistribution matrices, the released version of `gis2/3v4_0.rmf` were used. Spectral fits were performed with XSPEC v10.00 (Arnaud 1996).

2.5. *Systematic Errors*

In summary, the constituents of the observed GIS events in each field can be classified into the following four components: (1) the unresolved CXB originating in the f.o.v., (2) X-rays from outside of the f.o.v., (3) the resolved sources to be eliminated, and (4) the NXB. As an example, we plotted each spectrum for the whole LSS field (including a-LSS) in figure 7. In this figure, the spectra of (d) − (e), (e), (f), and (b) correspond to those classifications, respectively. The LSS field is suitable for this purpose because of its large sky coverage and the unbiased field selection. The brightest source in the LSS is AX J131822+3347 with 2–10 keV flux of 1.3×10^{-12} erg cm^{-2} s^{-1}. The count rate of each component in the 0.7–7 (2–10) keV band is 0.055 (0.033), 0.052 (0.022), 0.011 (0.005), and 0.045 (0.047) count s^{-1} sensor^{-1}, respectively. Since there is a comparable fraction of the stray light or the NXB to the unresolved CXB, accuracy of their estimation (as well as the statistics) determines the errors of the resultant CXB parameters.

As mentioned in subsection 2.2, the reproducibility of the NXB is considered to be 3%, which must be carefully dealt with when comparing the CXB parameters from field to field. On the other hand, the estimation error of the stray light mainly acts as if the effective area of the XRT is over- or under-estimated in common among the sample fields; hence it does not matter severely in a field-to-field comparison. As mentioned in subsection 2.4, because the stray-light estimation is considered to be accurate to within $\pm 10\%$ of the CXB

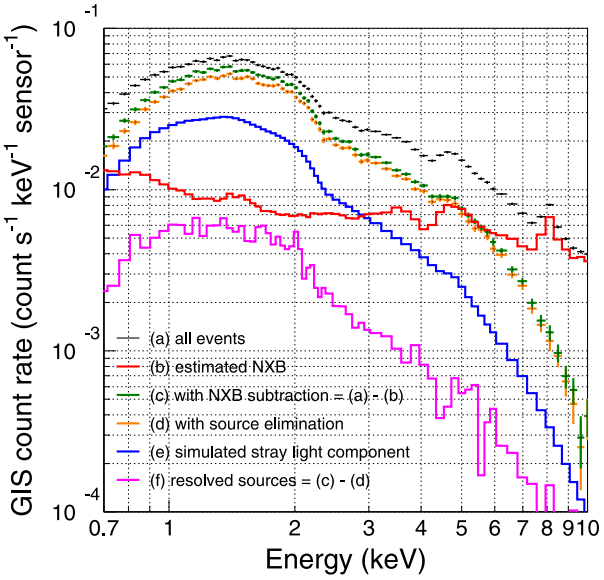

Fig. 7. Comparison of the spectral components for the LSS field when accumulated within a radius of 20 mm ($\simeq 20'$) from the optical axis of each GIS sensor. The spectra of all the pointings and both GIS sensors are summed up. From upper to lower (at 8 keV), each spectrum represents: (a) all events obtained in the LSS field after the data screening described in subsection 2.2; (b) the NXB spectrum estimated in the way as described in subsection 2.2; (c) the LSS spectrum after the NXB subtraction, i.e. (a) − (b); (d) the LSS spectrum after the source elimination described in subsection 2.3, in which the reduced fraction of 85.3% for the sky coverage is corrected; (e) the simulated component of the stray light which comes from the outside of the accumulation radius of 20 mm ($\simeq 20'$) from the respective optical axes; (f) the summed spectrum of the resolved sources, i.e. (c) − (d).

intensity, one should only pay attention to comparing our results on the absolute CXB intensity with those of other satellites.

3. Spectral Results

3.1. Individual Fields

In the first place, all the 91 spectra were fitted with a single power-law model. The interstellar absorption $N_{\rm H}$ were fixed to the Galactic values, which range from $0.8 \times 10^{20}\,{\rm cm}^{-2}$ to $22.3 \times 10^{20}\,{\rm cm}^{-2}$ (Dickey, Lockman 1990), and are listed in table 1. When we tried to fit the entire energy band (0.7–10 keV) with the free photon index, Γ, there remained a significant excess below ~ 2 keV in most of the 91 fields. The reduced χ^2 values showed a progressive improvement as the low-energy region was gradually cut out from the spectral fit. Two examples of the spectra are shown in the top panels of figure 8. Limiting the fitted energy range to be 2–10 keV, an average power-law photon index of $\Gamma^{\rm hard} = 1.400 \pm 0.008$ ($1\,\sigma$ error) with a standard deviation of 0.054 was obtained for the 91 sample fields. This $\Gamma^{\rm hard}$ agrees well with the previous results from *ASCA* (Gendreau et al. 1995; Miyaji et al. 1998) and from non-imaging measurements, such as *HEAO 1* A-2 (Marshall et al. 1980).

The existence of a soft excess has also been noticed in previous spectral studies, e.g. *ROSAT* (Hasinger 1992), *BBXRT* (Jahoda et al. 1992), and *ASCA* (Gendreau et al. 1995). The present analysis shows that the excess component is clearly seen in most of the 91 fields in the energy range below 2 keV. Such a wide-spread detection of spectral data and the intensity variation of the soft component, as shown in figure 8, is a newly found feature; the results would supplement the soft X-ray information obtained with the *ROSAT* all-sky survey. The variation amplitude of the soft component is roughly $1 \times 10^{-8}\,{\rm erg\,cm^{-2}\,s^{-1}\,sr^{-1}}$. This is a factor-of-three higher than the level which can be accounted for by the change of the Galactic $N_{\rm H}$ between the maximum and the minimum. To fit the 0.7–10 keV spectra in a consistent way, we need an additional spectral model for the soft component. For this, we have tried (1) power-law and (2) MEKAL models. In both cases, the soft and the hard components were absorbed by the same Galactic $N_{\rm H}$.

For the double power-law fit, the data were unable to simultaneously constrain the 2 spectral slopes in some fields. In fact, some of the fit showed a negative slope for the hard component, which seriously conflicts with the established value of $\Gamma^{\rm hard} \simeq 1.4$. We, therefore, fixed the slope of the hard component at 1.4. The fit for the 91 spectra then gave an average power-law photon index for the soft component, $\Gamma^{\rm soft} = 5.76 \pm 0.04$ ($1\,\sigma$ error) with a standard deviation of 0.33. Spectral examples are shown in the middle panels of figure 8, indicating a significant improvement in the fit for the IRAS 19245−7245 field. The slope of $\Gamma^{\rm soft} \sim 6$, however, indicates a steep rise in the soft band, and would imply a very strong emission in the *ROSAT* band unless some low-energy cut off is present. This behavior may have resulted from the power-law modeling of the soft component, and it seems to complicate the analysis procedure. Our analysis of the Lockman Hole field, which has been extensively studied from other satellites, also yielded a rather steep value of $\Gamma^{\rm soft} = 6.0^{+0.7}_{-0.6}$ (90% confidence level) compared to $\Gamma \sim 2.1$ obtained from *ROSAT* PSPC (Hasinger 1992).

As the origin of the soft excess, two possibilities are implied from *ROSAT* observations (Kerp 1994). One component is probably associated with the Galactic halo, and the other with the Local Hot Bubble (LHB). In Miyaji et al. (1998) using both the *ROSAT* PSPC and the *ASCA* GIS + SIS data, these components were fitted with two thermal models, and each plasma temperature was derived to be ~ 0.14 keV and ~ 0.07 keV, respectively. However, it is hard for *ASCA* GIS to detect these components separately, due to its limited sensitivity at the low-energy band. We therefore applied one thermal MEKAL model (Liedahl et al. 1995) for these soft thermal components. Following the fit with the double power-law model, we again fixed $\Gamma^{\rm hard}$ at 1.4, $N_{\rm H}$ at the Galactic values and the metal abundance at 1 solar. The average temperature kT of the thermal component was obtained to be 0.39 ± 0.03 keV ($1\,\sigma$) with a standard deviation of 0.26 keV. Some examples of the spectral fit are shown in the bottom panels of figure 8.

We then fixed the plasma temperature, kT, at several values between 0.14 and 0.7 keV. The former value has been indicated by many previous measurements; recent examples are Miyaji et al. (1998) mentioned above, and *ROSAT*/PSPC + rocket CCD experiments (Mendenhall, Burrows 2001). The latter value is implied by *BeppoSAX*/LECS (Parmar et al. 1999), although

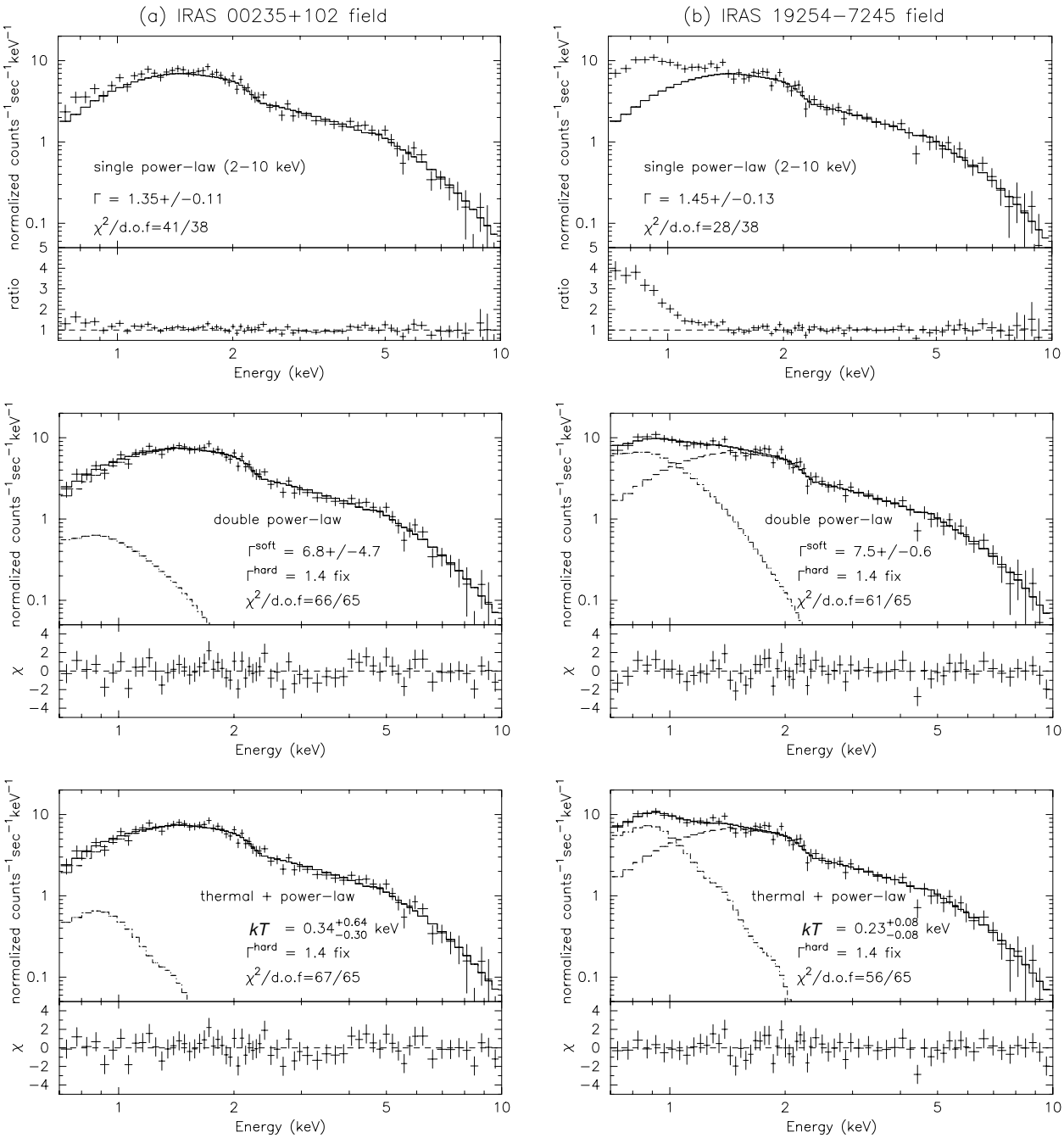

Fig. 8. Two examples of the energy spectra after the point source elimination taken in (a) IRAS 00235+102 field and (b) IRAS 19254−7245 field. The top, middle, and bottom panels show spectral fits with single power-law, double power-law, and soft thermal plus power-law models, respectively. In each panel, the upper diagram shows the data (crosses) fitted with each model (solid lines), and the lower diagram indicates the goodness of the fit.

they say that such a high temperature was caused by inadequate modeling. As can be seen in the distribution of reduced χ^2 in figure 9, the temperature range for the soft thermal component is not well constrained, mainly due to the limitation in the low-energy sensitivity of GIS. In order to examine the field-to-field fluctuation, we used a common kT fixed at the average value, 0.4 keV. The results of the spectral fits are listed in table 2.

3.2. *Integrated Spectrum*

The integrated spectrum for all 91 fields was constructed in order to look into the fine spectral features. The total integration time amounted to 4.2 Ms and the spectrum is shown in figure 10, where the Galactic absorption, $N_{\rm H}$, was fixed at $4.0 \times 10^{20}\,{\rm cm}^{-2}$, which is the average value weighted by the exposure time. The fitting results for the integrated spectrum are listed in table 3, as well as those for the whole LSS field (including a-LSS), because the LSS is a good example of

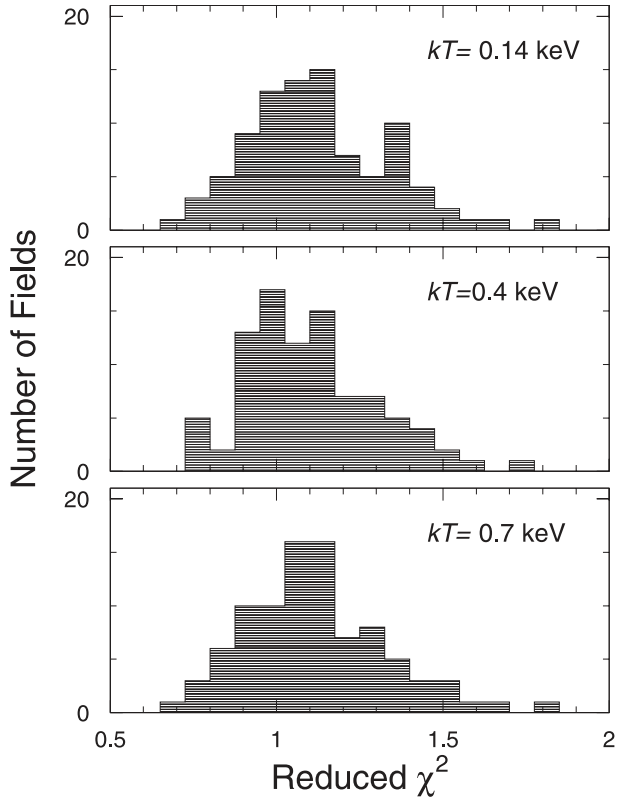

Fig. 9. Distribution of the reduced χ^2 for spectral fits with three different models of the soft component. The plasma temperatures of the soft thermal component are indicated in each panel.

the so-called blank sky. The average $\Gamma^{\rm hard}$ was obtained to be 1.411 ± 0.007 (90% confidence level). The χ^2 value was 175 for 65 degrees of freedom.

The residuals suggest some systematic feature above 8 keV, characterized by an intensity drop of $\lesssim 30\%$. However, the systematic error of the NXB intensity is $\sim 3\%$, as mentioned earlier, and the panels in figure 10 show that the residuals are very much reduced when the NXB level is varied by -3%. The cutoff feature is, therefore, not significant considering the error of the NXB level. The night-earth spectrum in figure 7 shows a Cu-K line around 8 keV, which is from the gas support grids of GIS. However, this line is clearly subtracted in the integrated spectra. The edge-like feature around 4.7 keV corresponds to the L-edge energy of xenon, which is the detector gas of GIS. In summary, we should say conservatively that the present GIS data do not indicate any significant deviation of the CXB spectrum from the nominal power-law spectrum in the energy range above 2 keV.

In order to check the contribution of bright sources in the GIS f.o.v., integrated spectra without source elimination were fitted similarly. These results are also shown in table 3. The photon index, $\Gamma^{\rm hard}$, seems not to be changed by applying the source elimination, while $F_{\rm X}^{\rm hard}$ is significantly affected by $\sim 13\%$ for the sample fields. This fraction is $\sim 9\%$ for the LSS, smaller than the former. This is because the AMSS fields contain brighter sources, which are often the target itself, than the LSS. Since the intensities after the source elimination agree well with each other, we can safely state that the source elimination worked well.

3.3. Correlations between Spectral Parameters

The correlations between the spectral parameters obtained in subsection 3.1 are shown in figures 11 and 12. There seems to be some correlation between $F_{\rm X}^{\rm soft}$ and $F_{\rm X}^{\rm hard}$ with a large relative amplitude in the variation of $F_{\rm X}^{\rm soft}$ ($1\,\sigma = 52^{+4}_{-5}\%$). $F_{\rm X}^{\rm soft}$ does not show a negative correlation with $N_{\rm H}$, which has been observed in very soft X-rays (e.g. Bowyer et al. 1968; Tanaka, Bleeker 1977). On the other hand, a clear anti-correlation is seen between $\Gamma^{\rm hard}$ and $F_{\rm X}^{\rm hard}$. The spectral fit for individual field indicates a systematic correlation between the parameters, as shown in the right panel of figure 12, in the sense that $\Gamma^{\rm hard}$ becomes smaller for a higher $F_{\rm X}^{\rm hard}$. However, the total range of the scatter is larger than the statistical error. We, therefore, conclude there is a systematic tendency between $F_{\rm X}^{\rm hard}$ and $\Gamma^{\rm hard}$. This correlation suggests that sources contributing to the fluctuation of the CXB at a level of $10^{-13}\,{\rm erg\,cm^{-2}\,s^{-1}}$ have relatively hard spectra.

4. Large-Scale Distribution

The present data are useful for looking at the all-sky distribution of the CXB with good sensitivity after point-source elimination. We examine here the large-scale distribution of both the soft and hard components.

4.1. Distribution in Our Galaxy

We first consider the spatial distribution of the soft and hard components in our Galaxy. The spectrum in each field was sorted with the Galactic latitude, b, and the longitude, l, and summed up in each cell. The spatial distributions are shown in figure 13. In this plot, the data were binned into 10° steps in b and 30° steps in l, respectively. In plotting the distribution along l, an additional condition of $|b| < 60^\circ$ was also applied. The $N_{\rm H}$ values were averaged over the respective angular cells. The instrumental responses were also summed within each cell.

The soft component shows a nearly symmetric distribution around a peak at the Galactic Center. This feature clearly indicates that the soft component is a Galactic emission, and is likely to extend further into the low-energy range. To examine this, we compared the soft-component intensity with the RASS intensity, as shown in figure 14. The correlation with the *ROSAT*-3/4 keV + 1.5 keV map (Snowden et al. 1995, 1997) is generally good, suggesting that these enhancements are associated with the Galactic bulge and the North Polar Spur. We also looked into some specific fields characterized by strong soft components. For example, in the IRAS 19254−7245 field, the RASS data also indicate a relatively strong flux. This supports the above view that the soft component has its origin within our Galaxy.

In order to compare our results with previous studies, we fitted the observed (l, b) profiles of $F_{\rm X}^{\rm hard}$ and $F_{\rm X}^{\rm soft}$ with a finite radius disk model, which successfully modeled the 2–60 keV and 2–18 keV distributions observed with *HEAO 1* A-2 (Iwan et al. 1982) or *Ariel V* SSI (Warwick et al. 1980), respectively. In this model, there is no Galactic X-ray emission outside of a disk of radius $R_{\rm d}$, and the emission within $R_{\rm d}$ has

Table 2. Results of the spectral fits.*

Field ID	Field name	$N_{\rm H}$†	$\Gamma^{\rm hard}$	$F_{\rm X}^{\rm hard}$‡	$F_{\rm X}^{\rm soft}$§	χ^2	d.o.f.
1	b-LSS	1.1	$1.416^{+0.032}_{-0.032}$	$5.69^{+0.16}_{-0.16}$	$0.40^{+0.09}_{-0.09}$	88.0	65
2	c-LSS	1.1	$1.436^{+0.031}_{-0.032}$	$5.55^{+0.15}_{-0.15}$	$0.37^{+0.08}_{-0.09}$	65.7	65
3	d-LSS	1.1	$1.446^{+0.036}_{-0.036}$	$5.71^{+0.18}_{-0.18}$	$0.37^{+0.10}_{-0.11}$	65.9	65
4	DRACO	4.2	$1.393^{+0.048}_{-0.048}$	$5.60^{+0.23}_{-0.23}$	$0.50^{+0.12}_{-0.12}$	82.8	65
5	JUPITER	2.2	$1.503^{+0.080}_{-0.083}$	$5.52^{+0.39}_{-0.38}$	$0.32^{+0.22}_{-0.24}$	76.5	65
6	NEP FIELD	4.2	$1.328^{+0.037}_{-0.037}$	$5.78^{+0.18}_{-0.18}$	$0.62^{+0.09}_{-0.08}$	104.6	65
7	QSF 3	1.6	$1.342^{+0.045}_{-0.045}$	$6.20^{+0.24}_{-0.24}$	$0.39^{+0.12}_{-0.13}$	66.5	65
8	ARP 220	4.3	$1.352^{+0.074}_{-0.074}$	$5.84^{+0.37}_{-0.36}$	$1.45^{+0.20}_{-0.22}$	62.4	65
9	3C 368	9.1	$1.407^{+0.079}_{-0.078}$	$6.25^{+0.40}_{-0.40}$	$1.46^{+0.23}_{-0.22}$	96.6	65
10	IRAS F10214+4724	1.2	$1.349^{+0.035}_{-0.035}$	$6.41^{+0.19}_{-0.19}$	$0.57^{+0.11}_{-0.10}$	98.2	65
11	IRAS 09104	1.0	$1.215^{+0.075}_{-0.075}$	$7.00^{+0.47}_{-0.46}$	$0.43^{+0.19}_{-0.21}$	48.0	65
12	MNVTEST	1.8	$1.435^{+0.056}_{-0.055}$	$5.81^{+0.28}_{-0.27}$	$0.62^{+0.15}_{-0.17}$	67.7	65
13	SN 1986J	7.5	$1.540^{+0.044}_{-0.047}$	$6.46^{+0.25}_{-0.25}$	$0.98^{+0.15}_{-0.14}$	75.6	65
14	AO 0235+164	9.0	$1.379^{+0.066}_{-0.069}$	$5.95^{+0.36}_{-0.36}$	$0.17^{+0.16}_{-0.15}$	54.9	65
15	NGC 1614	6.1	$1.395^{+0.083}_{-0.077}$	$5.43^{+0.38}_{-0.38}$	$0.57^{+0.18}_{-0.20}$	91.7	65
16	NGC 1667	5.5	$1.410^{+0.068}_{-0.069}$	$5.99^{+0.35}_{-0.34}$	$0.99^{+0.20}_{-0.18}$	90.5	65
17	4C 41.17	10.4	$1.559^{+0.084}_{-0.085}$	$5.45^{+0.40}_{-0.38}$	$0.27^{+0.21}_{-0.19}$	73.0	65
18	NGC 3690	0.9	$1.338^{+0.077}_{-0.077}$	$5.59^{+0.38}_{-0.37}$	$0.42^{+0.18}_{-0.20}$	81.7	65
19	K416	1.8	$1.406^{+0.078}_{-0.079}$	$4.88^{+0.35}_{-0.35}$	$0.20^{+0.19}_{-0.17}$	62.6	65
20	NGC 4449	1.4	$1.361^{+0.065}_{-0.065}$	$5.67^{+0.33}_{-0.32}$	$0.47^{+0.18}_{-0.17}$	59.1	65
21	PHL 5200	5.2	$1.434^{+0.037}_{-0.040}$	$7.12^{+0.24}_{-0.24}$	$0.79^{+0.14}_{-0.12}$	74.7	65
22	NGC 4418	2.1	$1.315^{+0.069}_{-0.069}$	$6.25^{+0.37}_{-0.36}$	$0.70^{+0.18}_{-0.20}$	70.7	65
23	GSGP 4	1.9	$1.410^{+0.034}_{-0.033}$	$6.07^{+0.17}_{-0.17}$	$0.45^{+0.09}_{-0.10}$	63.5	65
24	DI PEG	4.0	$1.345^{+0.077}_{-0.076}$	$6.19^{+0.41}_{-0.40}$	$0.52^{+0.21}_{-0.20}$	80.0	65
25	PG 1404+226	2.1	$1.351^{+0.086}_{-0.083}$	$6.24^{+0.47}_{-0.45}$	$0.86^{+0.25}_{-0.23}$	73.8	65
26	IRAS 15307+325	2.0	$1.318^{+0.061}_{-0.060}$	$6.21^{+0.33}_{-0.17}$	$0.53^{+0.17}_{-0.16}$	47.8	65
27	Z SYSTEM	2.2	$1.421^{+0.036}_{-0.036}$	$5.77^{+0.18}_{-0.18}$	$0.33^{+0.09}_{-0.10}$	51.9	65
28	MG 2016+112	15.5	$1.426^{+0.038}_{-0.038}$	$6.29^{+0.20}_{-0.20}$	$1.11^{+0.10}_{-0.09}$	64.2	65
29	IRAS 20460+192	11.2	$1.436^{+0.080}_{-0.077}$	$5.91^{+0.39}_{-0.38}$	$1.16^{+0.19}_{-0.19}$	67.3	65
30	BLANK SKY	13.4	$1.433^{+0.076}_{-0.074}$	$5.93^{+0.37}_{-0.36}$	$0.70^{+0.18}_{-0.17}$	58.2	65
31	EPSILON CMA	14.8	$1.535^{+0.077}_{-0.075}$	$5.25^{+0.33}_{-0.32}$	$0.74^{+0.17}_{-0.16}$	86.1	65
32	OJ 287	3.0	$1.467^{+0.059}_{-0.058}$	$4.98^{+0.26}_{-0.25}$	$0.47^{+0.13}_{-0.14}$	82.5	65
33	RASS 1011+1736	3.2	$1.433^{+0.061}_{-0.061}$	$5.66^{+0.30}_{-0.29}$	$0.28^{+0.15}_{-0.17}$	74.1	65
34	XY LEO	3.3	$1.405^{+0.103}_{-0.105}$	$5.22^{+0.48}_{-0.46}$	$0.35^{+0.22}_{-0.25}$	78.6	65
35	Mrk 231	1.3	$1.378^{+0.034}_{-0.033}$	$5.92^{+0.17}_{-0.17}$	$0.34^{+0.09}_{-0.10}$	59.3	65
36	NGC 7320	7.9	$1.350^{+0.078}_{-0.077}$	$6.20^{+0.40}_{-0.39}$	$1.04^{+0.20}_{-0.19}$	79.9	65
37	CN LEO	2.9	$1.466^{+0.064}_{-0.064}$	$5.57^{+0.32}_{-0.31}$	$0.39^{+0.18}_{-0.17}$	61.0	65
38	Mrk 273	1.1	$1.396^{+0.085}_{-0.080}$	$4.78^{+0.36}_{-0.35}$	$0.71^{+0.19}_{-0.21}$	76.1	65
39	NGC 5135	4.6	$1.452^{+0.073}_{-0.072}$	$5.57^{+0.35}_{-0.34}$	$0.72^{+0.18}_{-0.20}$	74.3	65
40	Q1508+5714	1.5	$1.347^{+0.051}_{-0.050}$	$6.13^{+0.27}_{-0.27}$	$0.40^{+0.13}_{-0.14}$	57.5	65
41	GB 930704	5.2	$1.366^{+0.079}_{-0.080}$	$5.52^{+0.40}_{-0.39}$	$0.75^{+0.19}_{-0.22}$	62.9	65
42	NGC 4125	1.8	$1.372^{+0.074}_{-0.072}$	$5.95^{+0.38}_{-0.37}$	$0.49^{+0.21}_{-0.19}$	48.7	65
43	TXFS 1011+144	3.9	$1.363^{+0.069}_{-0.068}$	$5.79^{+0.35}_{-0.22}$	$0.39^{+0.17}_{-0.18}$	70.6	65
44	MS 1054.5−0321	3.6	$1.382^{+0.055}_{-0.055}$	$6.47^{+0.31}_{-0.30}$	$0.35^{+0.15}_{-0.16}$	70.2	65
45	CL 2236−04	4.0	$1.349^{+0.078}_{-0.077}$	$5.70^{+0.39}_{-0.24}$	$0.35^{+0.18}_{-0.20}$	82.4	65
46	PG 1247+267	0.9	$1.290^{+0.077}_{-0.075}$	$6.36^{+0.43}_{-0.42}$	$0.56^{+0.22}_{-0.21}$	74.0	65
47	NGC 4450	2.4	$1.445^{+0.077}_{-0.075}$	$6.04^{+0.40}_{-0.35}$	$0.66^{+0.21}_{-0.23}$	69.0	65
48	QSO CLUSTER	1.1	$1.460^{+0.033}_{-0.032}$	$5.97^{+0.17}_{-0.17}$	$0.31^{+0.09}_{-0.11}$	83.9	65
49	NGC 5084	8.2	$1.339^{+0.086}_{-0.085}$	$5.92^{+0.43}_{-0.42}$	$1.07^{+0.21}_{-0.20}$	69.1	65
50	SA 68	4.2	$1.379^{+0.054}_{-0.052}$	$5.85^{+0.27}_{-0.26}$	$0.54^{+0.13}_{-0.14}$	56.6	65

Table 2. (Continued)

Field ID	Field name	N_H†	Γ^{hard}	F_X^{hard}‡	F_X^{soft}§	χ^2	d.o.f.
51	Mrk 348	5.8	$1.317^{+0.079}_{-0.079}$	$5.82^{+0.40}_{-0.26}$	$0.31^{+0.17}_{-0.19}$	78.7	65
52	NGC 1332	2.2	$1.403^{+0.057}_{-0.058}$	$5.85^{+0.30}_{-0.29}$	$0.46^{+0.16}_{-0.15}$	62.0	65
53	PKS 0634−205	22.3	$1.299^{+0.081}_{-0.079}$	$6.38^{+0.41}_{-0.40}$	$0.89^{+0.16}_{-0.15}$	73.4	65
54	IRAS 20551−425	3.9	$1.524^{+0.081}_{-0.080}$	$5.49^{+0.38}_{-0.37}$	$0.59^{+0.22}_{-0.23}$	63.7	65
55	HS 1946+7658	7.6	$1.518^{+0.063}_{-0.063}$	$5.97^{+0.32}_{-0.31}$	$0.54^{+0.17}_{-0.18}$	48.7	65
56	RGH 12	1.5	$1.355^{+0.066}_{-0.065}$	$5.61^{+0.32}_{-0.16}$	$0.49^{+0.17}_{-0.16}$	59.0	65
57	UKMS 1	0.8	$1.408^{+0.055}_{-0.056}$	$5.83^{+0.28}_{-0.28}$	$0.33^{+0.15}_{-0.17}$	64.1	65
58	F568−06	2.0	$1.378^{+0.060}_{-0.064}$	$6.16^{+0.35}_{-0.33}$	$0.24^{+0.17}_{-0.19}$	60.9	65
59	NGC 7217	10.5	$1.548^{+0.063}_{-0.062}$	$5.25^{+0.28}_{-0.27}$	$0.52^{+0.15}_{-0.14}$	63.1	65
60	NGC 1672	2.3	$1.438^{+0.079}_{-0.081}$	$5.44^{+0.39}_{-0.38}$	$0.33^{+0.20}_{-0.23}$	76.1	65
61	BJS 855	4.0	$1.436^{+0.061}_{-0.061}$	$6.09^{+0.32}_{-0.32}$	$0.31^{+0.16}_{-0.18}$	72.9	65
62	PG 1148+549	1.2	$1.441^{+0.071}_{-0.071}$	$6.08^{+0.38}_{-0.37}$	$0.40^{+0.20}_{-0.23}$	61.1	65
63	IRAS 00317−2142	1.6	$1.439^{+0.076}_{-0.078}$	$5.82^{+0.40}_{-0.39}$	$0.34^{+0.21}_{-0.24}$	84.0	65
64	NGC 5005	1.1	$1.279^{+0.078}_{-0.077}$	$6.49^{+0.44}_{-0.43}$	$0.55^{+0.21}_{-0.22}$	72.6	65
65	NGC 5018	7.0	$1.373^{+0.064}_{-0.066}$	$6.04^{+0.35}_{-0.34}$	$0.94^{+0.17}_{-0.19}$	68.9	65
66	4C 38.41	1.0	$1.405^{+0.083}_{-0.082}$	$5.87^{+0.43}_{-0.42}$	$0.56^{+0.24}_{-0.23}$	66.5	65
67	AR UMa	1.8	$1.472^{+0.054}_{-0.050}$	$6.22^{+0.27}_{-0.28}$	$0.13^{+0.16}_{-0.13}$	64.5	65
68	PG 1114+445	1.8	$1.398^{+0.059}_{-0.061}$	$6.00^{+0.33}_{-0.31}$	$0.25^{+0.16}_{-0.17}$	78.1	65
69	HE 1104−1805	4.6	$1.467^{+0.077}_{-0.076}$	$5.75^{+0.39}_{-0.38}$	$0.44^{+0.20}_{-0.21}$	71.8	65
70	RX J1716.6+670	3.7	$1.371^{+0.055}_{-0.056}$	$5.75^{+0.28}_{-0.27}$	$0.29^{+0.13}_{-0.14}$	60.1	65
71	B2 1308+326	1.1	$1.402^{+0.081}_{-0.082}$	$5.57^{+0.41}_{-0.41}$	$0.26^{+0.23}_{-0.20}$	110.8	65
72	Q2345+007	3.8	$1.454^{+0.054}_{-0.053}$	$5.41^{+0.25}_{-0.25}$	$0.39^{+0.13}_{-0.14}$	61.6	65
73	IRAS 00235+102	5.1	$1.417^{+0.068}_{-0.064}$	$6.17^{+0.34}_{-0.35}$	$0.20^{+0.16}_{-0.18}$	66.7	65
74	NGC 612	1.8	$1.417^{+0.052}_{-0.051}$	$5.63^{+0.25}_{-0.25}$	$0.55^{+0.14}_{-0.13}$	95.1	65
75	CL 0024+17	4.2	$1.343^{+0.068}_{-0.063}$	$6.39^{+0.38}_{-0.37}$	$0.64^{+0.18}_{-0.20}$	65.9	65
76	NGC 315	5.9	$1.469^{+0.076}_{-0.077}$	$5.64^{+0.38}_{-0.37}$	$0.31^{+0.19}_{-0.21}$	91.2	65
77	MS 0302.7+1658	10.9	$1.566^{+0.049}_{-0.049}$	$4.97^{+0.21}_{-0.20}$	$0.31^{+0.10}_{-0.11}$	93.6	65
78	V 471 TAURI	15.8	$1.326^{+0.075}_{-0.074}$	$6.74^{+0.43}_{-0.41}$	$0.40^{+0.14}_{-0.16}$	87.8	65
79	RX J1802+1804	8.5	$1.383^{+0.054}_{-0.053}$	$6.63^{+0.30}_{-0.30}$	$0.94^{+0.14}_{-0.15}$	60.9	65
80	A548	1.9	$1.585^{+0.048}_{-0.047}$	$5.55^{+0.23}_{-0.22}$	$0.41^{+0.15}_{-0.14}$	57.5	65
81	IRAS 19254−7245	6.0	$1.353^{+0.081}_{-0.080}$	$5.83^{+0.39}_{-0.38}$	$2.47^{+0.24}_{-0.25}$	61.8	65
82	IRAS 07598+6508	4.3	$1.515^{+0.070}_{-0.070}$	$5.35^{+0.33}_{-0.32}$	$0.44^{+0.18}_{-0.19}$	68.2	65
83	HERC-1	2.4	$1.292^{+0.059}_{-0.055}$	$6.62^{+0.35}_{-0.34}$	$0.78^{+0.18}_{-0.16}$	86.7	65
84	IRAS 08572+3915	2.6	$1.417^{+0.081}_{-0.080}$	$6.03^{+0.42}_{-0.41}$	$0.46^{+0.24}_{-0.22}$	58.6	65
85	A851	1.2	$1.402^{+0.045}_{-0.045}$	$5.62^{+0.23}_{-0.22}$	$0.30^{+0.11}_{-0.13}$	70.4	65
86	NGC 7130	2.0	$1.466^{+0.077}_{-0.077}$	$5.25^{+0.36}_{-0.35}$	$0.42^{+0.21}_{-0.20}$	67.2	65
87	10303+7401	4.1	$1.468^{+0.064}_{-0.059}$	$6.16^{+0.32}_{-0.33}$	$0.17^{+0.18}_{-0.17}$	77.8	65
88	4C 06.41	2.8	$1.452^{+0.054}_{-0.055}$	$5.60^{+0.27}_{-0.26}$	$0.25^{+0.14}_{-0.14}$	74.1	65
89	M96	2.8	$1.486^{+0.062}_{-0.063}$	$5.36^{+0.30}_{-0.29}$	$0.26^{+0.18}_{-0.16}$	72.9	65
90	IC 2560	6.5	$1.305^{+0.066}_{-0.059}$	$6.74^{+0.37}_{-0.37}$	$0.51^{+0.17}_{-0.17}$	64.8	65
91	PG 0043+039	3.3	$1.393^{+0.049}_{-0.049}$	$5.95^{+0.25}_{-0.25}$	$0.36^{+0.13}_{-0.14}$	86.7	65
—	average‖	···	$1.412^{+0.007}_{-0.007}$	$5.85^{+0.04}_{-0.04}$	$0.51^{+0.03}_{-0.03}$	···	···
—	standard deviation♯	···	$0.055^{+0.005}_{-0.006}$	$0.38^{+0.03}_{-0.04}$	$0.26^{+0.02}_{-0.02}$	···	···

* Results from MEKAL plus power-law model fitting (see section 3). Error represents 90% confidence level. The temperature and abundance are fixed at $kT = 0.4$ keV and $Z = 1.0$ solar, respectively.

† Galactic absorption (10^{20} cm^{-2}) for both the power-law and the MEKAL components. Same as table 1.

‡ Flux of the power-law component (10^{-8} erg cm^{-2} s^{-1} sr^{-1}) in the 2–10 keV band.

§ Flux of the MEKAL component (10^{-8} erg cm^{-2} s^{-1} sr^{-1}) in the 0.5–2 keV band.

‖ Weighted average A_V and its 1σ error δA_V calculated with equations (7) and (8).

♯ Standard deviation $\sqrt{Sd^2}$ and its 1σ error, $\sqrt{Sd^2 \pm \delta Sd^2} - \sqrt{Sd^2}$, after the subtraction of statistical error calculated with equations (9) and (10).

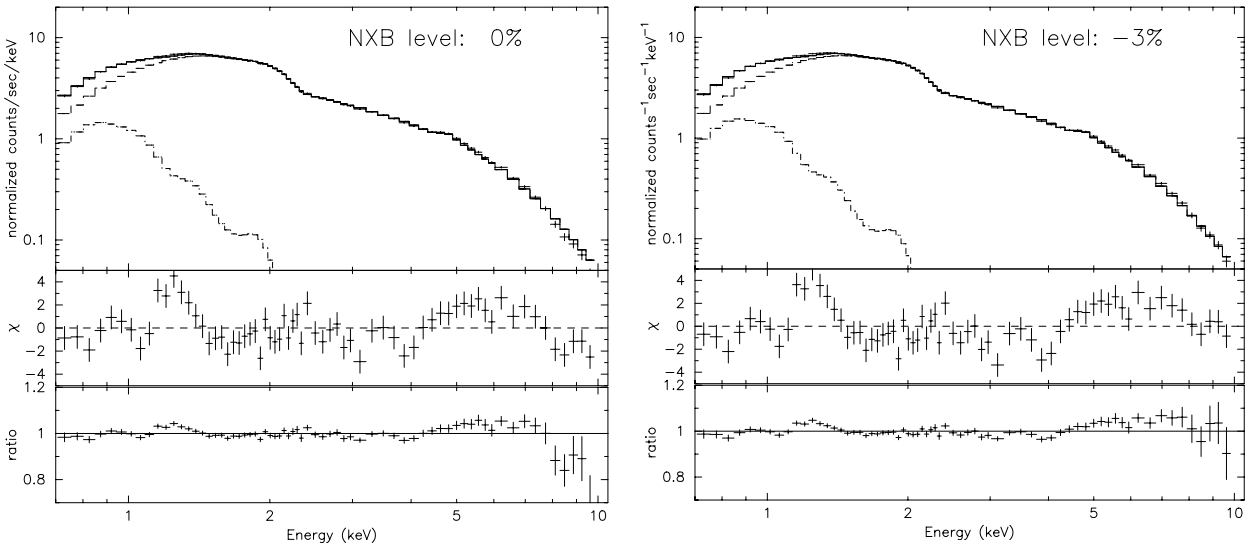

Fig. 10. Integrated pulse-height spectrum of the CXB for an exposure time of 4.2 Ms and a sky coverage of 40 deg^2. Each panel shows the data fitted with a 2-component model, the residual in unit of σ, and the data-to-model ratio. The left panel is for the nominal NXB subtraction, and the right one uses 3% reduced NXB.

Table 3. Fitting results for the integrated spectrum in the 91 sample fields and the whole LSS field (including a-LSS).

NXB (%)	Γ	F_X^{hard} (2–10 keV) (10^{-8} erg cm^{-2} s^{-1} sr^{-1})	F_X^{soft} (0.5–2 keV) (10^{-8} erg cm^{-2} s^{-1} sr^{-1})	χ^2/d.o.f.
Integrated spectrum with source elimination				
+3	$1.439^{+0.007}_{-0.007}$ (1.4 fix)	$5.72^{+0.04}_{-0.04}$ ($5.90^{+0.02}_{-0.02}$)	$0.49^{+0.02}_{-0.02}$ ($0.55^{+0.01}_{-0.02}$)	196/65 (275/66)
0	$1.411^{+0.007}_{-0.007}$ (1.4 fix)	$5.92^{+0.04}_{-0.04}$ ($5.97^{+0.02}_{-0.02}$)	$0.53^{+0.02}_{-0.02}$ ($0.55^{+0.01}_{-0.02}$)	175/65 (182/66)
−3	$1.386^{+0.006}_{-0.007}$ (1.4 fix)	$6.11^{+0.04}_{-0.04}$ ($6.04^{+0.02}_{-0.02}$)	$0.57^{+0.02}_{-0.02}$ ($0.54^{+0.02}_{-0.01}$)	199/65 (211/66)
Integrated spectrum without source elimination				
+3	$1.431^{+0.006}_{-0.006}$ (1.4 fix)	$6.61^{+0.03}_{-0.03}$ ($6.77^{+0.02}_{-0.02}$)	$0.61^{+0.02}_{-0.02}$ ($0.66^{+0.01}_{-0.01}$)	243/65 (322/66)
0	$1.407^{+0.006}_{-0.005}$ (1.4 fix)	$6.80^{+0.03}_{-0.03}$ ($6.84^{+0.02}_{-0.02}$)	$0.65^{+0.02}_{-0.02}$ ($0.66^{+0.01}_{-0.01}$)	239/65 (243/66)
−3	$1.385^{+0.006}_{-0.006}$ (1.4 fix)	$6.99^{+0.03}_{-0.03}$ ($6.91^{+0.02}_{-0.02}$)	$0.68^{+0.02}_{-0.02}$ ($0.66^{+0.01}_{-0.01}$)	286/65 (306/66)
LSS spectrum with source elimination				
+3	$1.447^{+0.017}_{-0.017}$ (1.4 fix)	$5.51^{+0.08}_{-0.08}$ ($5.71^{+0.04}_{-0.04}$)	$0.32^{+0.05}_{-0.05}$ ($0.39^{+0.04}_{-0.04}$)	75/65 (95/66)
0	$1.418^{+0.017}_{-0.017}$ (1.4 fix)	$5.70^{+0.08}_{-0.08}$ ($5.78^{+0.04}_{-0.04}$)	$0.36^{+0.04}_{-0.05}$ ($0.39^{+0.04}_{-0.04}$)	72/65 (75/66)
−3	$1.392^{+0.016}_{-0.017}$ (1.4 fix)	$5.88^{+0.08}_{-0.08}$ ($5.85^{+0.04}_{-0.04}$)	$0.40^{+0.05}_{-0.04}$ ($0.39^{+0.04}_{-0.04}$)	78/65 (78/66)
LSS spectrum without source elimination				
+3	$1.469^{+0.015}_{-0.015}$ (1.4 fix)	$5.97^{+0.08}_{-0.07}$ ($6.29^{+0.04}_{-0.04}$)	$0.42^{+0.04}_{-0.05}$ ($0.54^{+0.04}_{-0.03}$)	75/65 (135/66)
0	$1.442^{+0.015}_{-0.014}$ (1.4 fix)	$6.17^{+0.08}_{-0.07}$ ($6.36^{+0.04}_{-0.04}$)	$0.46^{+0.05}_{-0.04}$ ($0.54^{+0.03}_{-0.04}$)	70/65 (93/66)
−3	$1.417^{+0.015}_{-0.014}$ (1.4 fix)	$6.35^{+0.08}_{-0.08}$ ($6.43^{+0.04}_{-0.04}$)	$0.50^{+0.05}_{-0.04}$ ($0.53^{+0.04}_{-0.03}$)	75/65 (80/66)

Note. Values in parentheses are results when Γ^{hard} is fixed to 1.4. Errors are 90% confidence levels. Systematic errors are also examined by changing the NXB levels.

an exponential dependence on the vertical distance above the plane characterized by a scale height parameter, h. The total X-ray intensity, $I_{tot}(l, b)$, is given by

$$I_{tot}(l,b) = I_0 + E\frac{h/R_g}{\sin|b|}\left[1 - \exp\left(-\frac{\tan|b|}{h/R_g}x\right)\right], \quad (2)$$

in which $x = \cos l + \sqrt{(R_d/R_g)^2 - \sin^2 l}$, where I_0 is the average isotropic extragalactic emission assumed in this model, E is the normalization constant for the Galactic emission, and R_g is the distance to the Galactic Center. When we fit the observed distribution with this model, additional errors of 5.5% and 4.0% times F_X^{hard} were added to F_X^{hard} and F_X^{soft}, respectively,

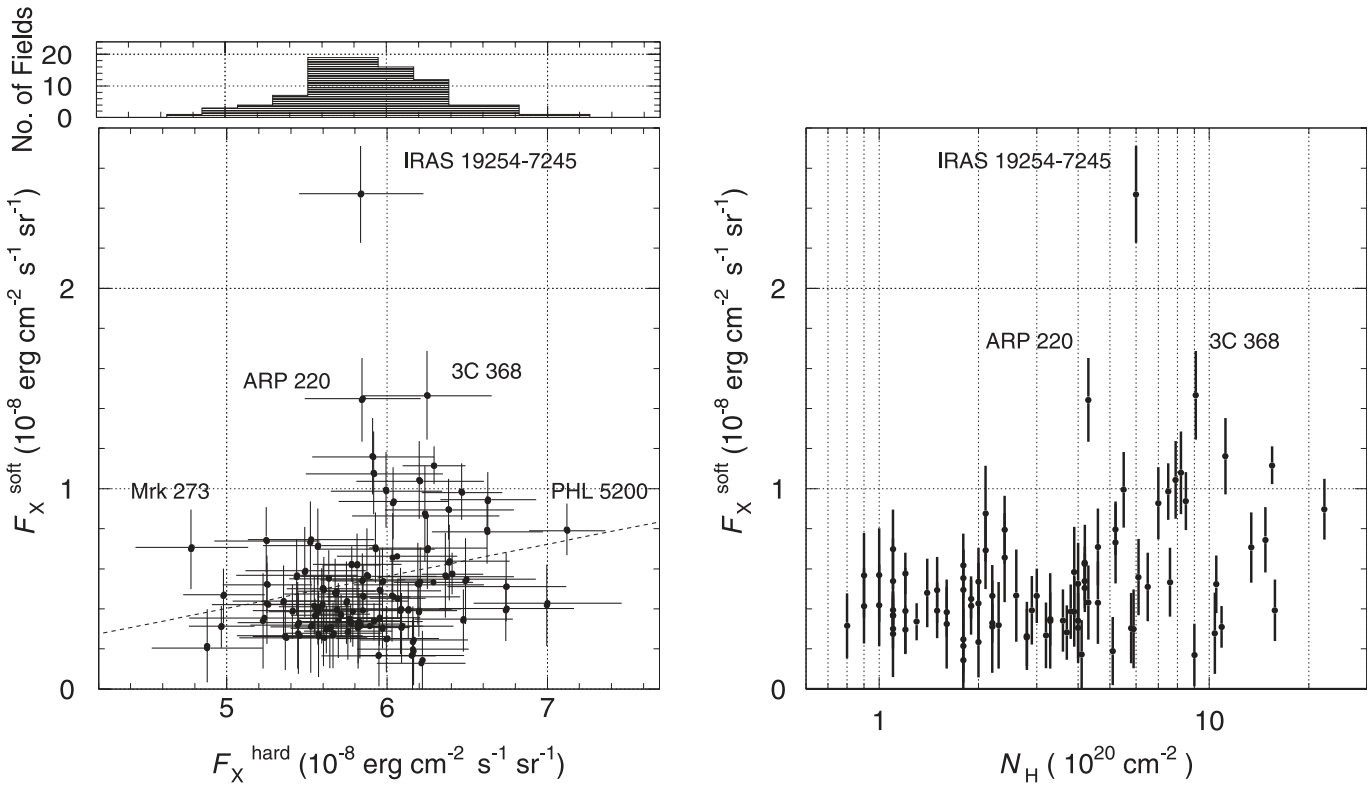

Fig. 11. The left panel shows correlations between F_X^{hard} and F_X^{soft}, with the distribution histogram of F_X^{hard} plotted in the top panel. The dashed line indicates the best-fit linear relation. The right panel shows the correlation between F_X^{soft} and N_H. In both panels, the error bars represent the 90% confidence levels.

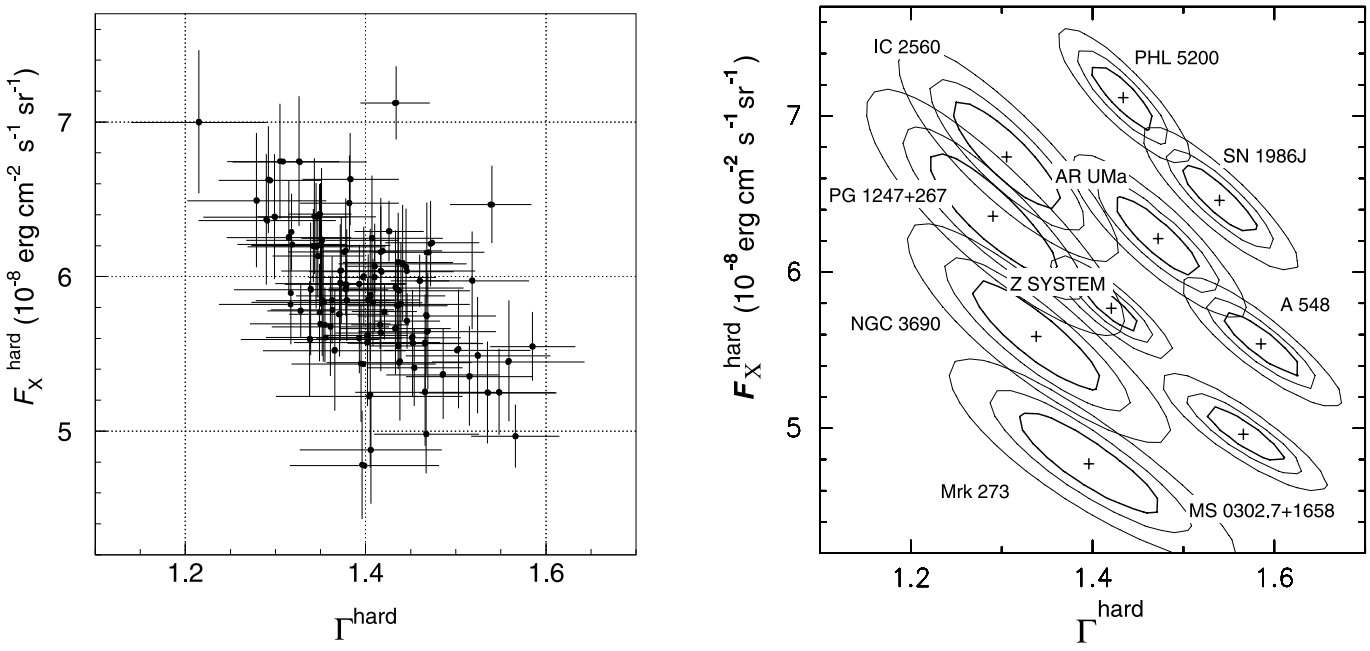

Fig. 12. The left panel shows correlations between F_X^{hard} and Γ^{hard}, and the right panel shows examples of confidence contours for several fields. The error bars represent the 90% errors for a single parameter ($\Delta\chi^2 = 2.70$). The contours correspond to $\Delta\chi^2$ of 2.3, 4.6, and 9.2.

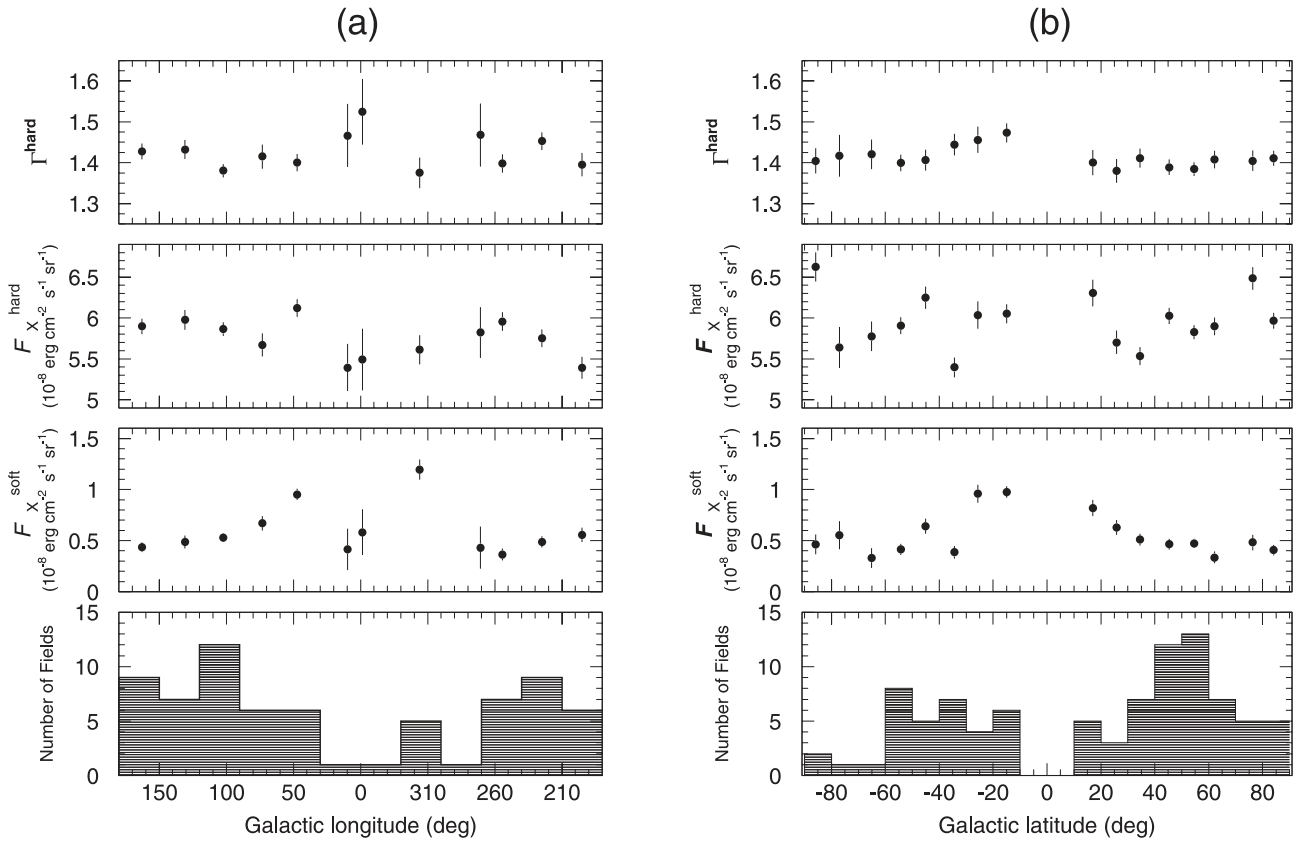

Fig. 13. Distribution of the spectral parameters in our Galaxy based on the fits of spatially sorted pulse-height spectra. Left and right panels are for the Galactic longitude (l) and latitude (b), respectively. The four rows from top to bottom show $\Gamma^{\rm hard}$, $F_{\rm X}^{\rm hard}$, $F_{\rm X}^{\rm soft}$, and number of fields, respectively. The error bars correspond to the 90% confidence levels.

in order to adjust the reduced χ^2 unity. This procedure is justified because the observed extragalactic CXB intensity, itself, would scatter intrinsically by about this amount, as described in section 5.

The $F_{\rm X}^{\rm soft}$ distribution was fitted well by the finite radius disk model, although there is a strong correlation between the scale height h and the disk radius $R_{\rm d}$, as shown in figure 15a. The best-fit parameters are $I_0 = (0.01 \pm 0.10) \times 10^{-8}\,{\rm erg\,cm^{-2}\,s^{-1}\,sr^{-1}}$, $E = (1.9 \pm 0.9) \times 10^{-8}\,{\rm erg\,cm^{-2}\,s^{-1}\,sr^{-1}}$, $h = (0.19 \pm 0.08) R_{\rm g}$, and $R_{\rm d} = (1.15 \pm 0.23) R_{\rm g}$ (errors are 1σ), with χ^2/d.o.f. = 107.3/87. Since I_0 is consistent to be zero and $E \gg I_0$, we can say that the soft thermal component is almost entirely a Galactic emission. The absorption-corrected flux of the hard power-law component in the 0.5–2 keV energy band is $2.07 \times 10^{-8}\,{\rm erg\,cm^{-2}\,s^{-1}\,sr^{-1}}$ if we assume the average photon index of $\Gamma^{\rm hard} = 1.412$ over the whole energy range. Therefore, the contribution of the Galactic component in the 0.5–2 keV band is calculated to be 49% at $(l, |b|) = (0°, 20°)$, and 18% at $|b| = 90°$, respectively.

For the hard power-law component, we could hardly constrain the parameters for the $F_{\rm X}^{\rm hard}$ distribution by fitting it with the finite radius disk model, as shown in figure 15b. We therefore fixed the parameters at $R_{\rm d} = 2.8 R_{\rm g}$ and $h = 0.73 R_{\rm g}$, which were the best-fit values for the *HEAO 1* A-2 observation (Iwan et al. 1982). These values are inside of the $\chi^2 < \chi^2_{\rm min} + 1$ region in figure 15b. We then obtained $E = 3.7 \pm 2.3\%$ of

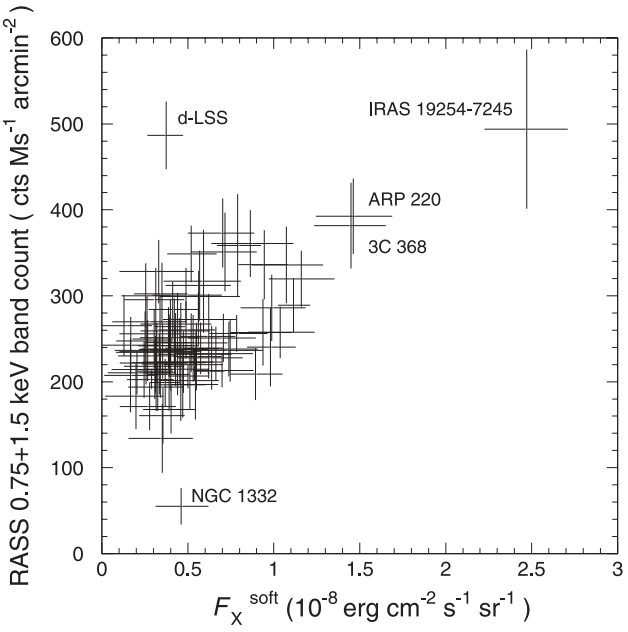

Fig. 14. Correlation between $F_{\rm X}^{\rm soft}$ and the RASS count in the 3/4 keV + 1.5 keV band for each sample field. The RASS count is averaged over the $36' \times 36'$ region centered in the *ASCA* field.

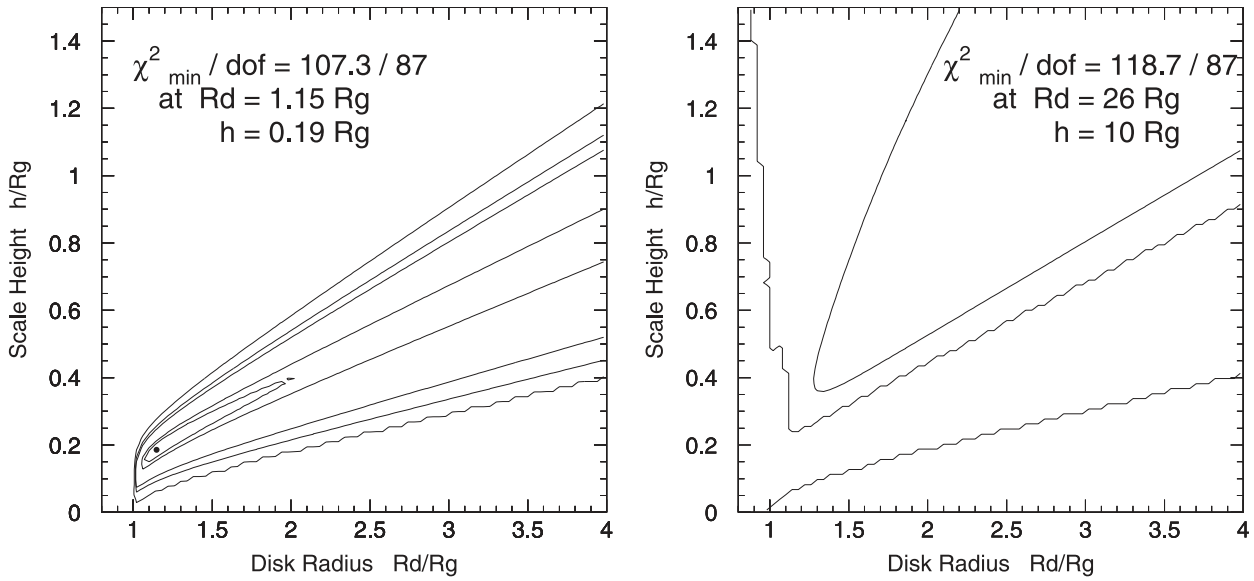

Fig. 15. Confidence contours between the scale height (h/R_g) and disk radius (R_d/R_g) parameters of the finite radius disk model for the F_X^{soft} (left panel) and F_X^{hard} (right panel). The contour levels are χ^2_{min} + 0.5, +1.0, +4.61 (90%), +5.99 (95%), +9.21 (99% confidence range), respectively, from inner to outer. The filled circle in the left panel represents the χ^2_{min} position. For the right panel, the χ^2_{min} position is out of the panel.

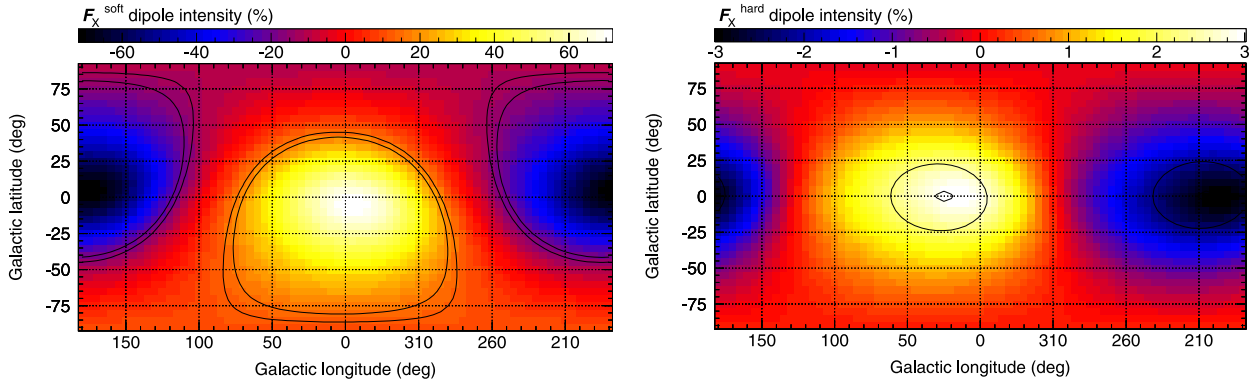

Fig. 16. Distributions of dipole amplitude for F_X^{soft} (left) and F_X^{hard} (right) plotted in the Galactic coordinate. The relative amplitude is indicated by color bars. The contours correspond to the 90% and 95% confidence levels from outer to inner, where the dipole amplitude has a non-zero value.

$I_0 = (5.61 \pm 0.13) \times 10^{-8}$ erg cm^{-2} s^{-1} sr^{-1} (errors are 1σ), which agrees well with the *HEAO 1* A-2 value of $E = 3.14\%$. Hence, the Galactic component in the 2–10 keV band has a low significance. Using our best-fit values, the Galactic contribution in the 2–10 keV band was calculated to be 7.1% at $(l, |b|) = (0°, 20°)$, and 2.7% at $|b| = 90°$, although the errors are large. These estimations are again consistent with the very early results from *Ariel V* SSI (Warwick et al. 1980), 7.2% and 2.5%, respectively. We can also compute the Galactic contribution to the CXB fluctuation to be $1\sigma = 1.2\%$, based on the best-fit model. This is much smaller than the observed fluctuation of $1\sigma = 6.49^{+0.56}_{-0.61}\%$ (table 2).

4.2. *Dipole Fitting*

Aiming at detecting another spatial structure than the Galactic component, we next tried to fit the intensity distribution with a dipole model, as a first-order approximation of the spherical harmonics. The dipole intensity distribution is expressed by

$$\frac{F_X(\Theta) - \overline{F_X}}{\overline{F_X}} = I \cos\Theta, \quad (3)$$

where Θ is the angle between the center of each field and the assumed pole direction, I is the amplitude of the dipole, and $\overline{F_X}$ is the average of the observed flux. As for the pole direction, we searched for all directions over the sky with a step size of 5°. The hard and soft components were examined separately, and the errors in the fits were calculated in the same way as in the previous subsection. Figure 16 shows the distributions of the best-fit dipole amplitude in the Galactic coordinate.

As expected from the previous subsection, the soft component (F_X^{soft}) indicates a strong peak near the Galactic Center at $(l, b) = (-5°, -5°)$ with a relative amplitude of $72 \pm 13\%$ (1σ error). The hard component (F_X^{hard}) also suggests some dipole

emission with a maximum amplitude of $3.0 \pm 1.6\%$ (1σ error) at $(l, b) = (15^\circ, 0^\circ)$. There are slight shifts from the Galactic Center to the positions of the maximum dipole amplitude, towards the south direction for the $F_{\rm X}^{\rm soft}$ and east for the $F_{\rm X}^{\rm hard}$. This is presumably due to the influences of the brightest fields, the IRAS 19254 field at $(l, b) = (322.^\circ4, -28.^\circ7)$ for the $F_{\rm X}^{\rm soft}$, and the PHL 5200 field at $(59.^\circ1, -49.^\circ6)$ for the $F_{\rm X}^{\rm hard}$. When these fields are removed in the dipole fittings, the directions of the shift change.

Since the Galactic contribution is too much dominant, we further tried a dipole fitting after subtracting the best-fit dipole model with its pole directed to the Galactic Center. Then, the residuals were consistent with no dipole emission at the 90% confidence level in the whole sky, for both $F_{\rm X}^{\rm soft}$ and $F_{\rm X}^{\rm hard}$. According to the Cosmic Microwave Background (CMB) dipole (Lineweaver et al. 1996), a dipole amplitude of 0.42% towards $(l, b) = (264^\circ, 48^\circ)$ is expected due to the so-called Compton–Getting (CG) effect. The CG dipole originates in our local motion with respect to the distant X-ray frame, which is expected to agree with the direction and velocity determined from the CMB dipole. There is some evidence that the dipolar emission also exists in the X-ray band, e.g. Plionis and Georgantopoulos (1999) with the 1.5 keV map of the *ROSAT* all-sky survey, Scharf et al. (2000) with the *HEAO 1* A-2 all-sky survey in 2–10 keV. Our dipole amplitudes in this direction after the subtraction is $-8.1 \pm 8.1\%$ (1σ error) for the $F_{\rm X}^{\rm soft}$ and $-0.5 \pm 1.0\%$ (1σ error) for the $F_{\rm X}^{\rm hard}$. It is almost impossible to detect such a small level of the dipole ($I = 0.42\%$) with our data, because the standard deviations of the observed intensity are much higher (52% and 6.5% for the $F_{\rm X}^{\rm soft}$ and $F_{\rm X}^{\rm hard}$, respectively) and the number of sample fields is limited to 91.

5. CXB Intensity and Fluctuations

The present survey consists of 91 fields distributing in the whole sky, and provides an excellent database. Regarding the field-to-field fluctuation of the hard component ($F_{\rm X}^{\rm hard}$), we evaluated the contribution from our Galaxy to be 1.2% in the previous section, which is much smaller than the observed fluctuation of $1\sigma = 6.49^{+0.56}_{-0.61}\%$ (table 2). Therefore, the origin of the CXB is considered to be mostly due to the extra-galactic one, and its distribution reflects a beam-to-beam fluctuation of X-ray sources in the observed field. In this section, we will try to constrain the $\log N - \log S$ relation of X-ray sources in the flux range, $S \lesssim 2 \times 10^{-13}\,{\rm erg\,cm^{-2}\,s^{-1}}$ at 2–10 keV. We compare this fluctuation with simulations, and constrain the $\log N - \log S$ source distribution.

5.1. log N–log S Relation

In order to examine the observed fluctuation compared with the expected level from an assumed $\log N - \log S$ relation, a detailed simulation including all of the instrumental characteristics is essential. In the *ASCA* data, there is a significant flux contribution ($\sim$ 35–45%; see subsection 2.5) from outside of the f.o.v. in the observed CXB intensity. Inside the f.o.v., discrete sources brighter than $S \approx 2 \times 10^{-13}\,{\rm erg\,cm^{-2}\,s^{-1}}$ (2–10 keV) were eliminated, whereas we could not exclude brighter sources outside of the f.o.v. We only picked up extremely bright sources, which may influence the CXB intensity by more than 2.5% based on the *HEAO 1* A-1 catalog and the RASS-BSC, and discarded the associated fields (subsection 2.3). We conducted a number of simulations to effectively constrain the intensity distribution and spectral properties of the incident sources, including all of these systematic effects.

We first assumed a certain $\log N - \log S$ relation which defines the intensity distribution of X-ray sources in the sky. The differential form of the flux (S) vs. number (n) relation is expressed using a normalization k and a slope γ as

$$n(S) = -\frac{dN(>S)}{dS} = \begin{cases} 0 & (S < S_{\rm min}), \\ kS^{-\gamma} & (S_{\rm min} < S), \end{cases} \tag{4}$$

where the notation $N(>S)$ means the number density of sources brighter than S per steradian. The γ value equals 2.5 in the Euclidean Universe, which is a good approximation, at least in the range of $S \gtrsim 10^{-13}\,{\rm erg\,cm^{-2}\,s^{-1}}$ (2–10 keV). Then, the integrated form is given as

$$N(>S) = \begin{cases} \dfrac{k}{\gamma - 1} S_{\rm min}^{-\gamma+1} & (S < S_{\rm min}), \\ \dfrac{k}{\gamma - 1} S^{-\gamma+1} & (S_{\rm min} < S). \end{cases} \tag{5}$$

The CXB intensity in the flux range of $S < S_0$ is calculated as

$$F(S_0) = \int_{S_{\rm min}}^{S_0} n(S) S\, dS = \frac{k}{\gamma - 2}(S_{\rm min}^{-\gamma+2} - S_0^{-\gamma+2}). \tag{6}$$

We tentatively adopt $k = k_0 = 1.58 \times 10^{-15}$ and $\gamma = \gamma_0 = 2.5$, which give a reasonable source density of $N(>S_0) = N_0 = 1.18 \times 10^4\,{\rm sr^{-1}}$ at $S = S_0 = 2.0 \times 10^{-13}\,{\rm erg\,cm^{-2}\,s^{-1}}$ (2–10 keV). The $S_{\rm min}$ value is determined to be $2.52 \times 10^{-15}\,{\rm erg\,cm^{-2}\,s^{-1}}$ (2–10 keV), using $F(S_0) = F_0 = 5.59 \times 10^{-8}\,{\rm erg\,cm^{-2}\,s^{-1}\,sr^{-1}}$ (2–10 keV) which matches the observed value (subsection 5.4). In figure 17a, the assumed $\log N - \log S$ relation with these tentative parameters are shown by the solid line (Model 1).

5.2. Simulation

We next generated a number of skies, where point sources are randomly spread out up to the off-axis angle of $2.^\circ5$, with their source density and flux distribution following the assumed $\log N - \log S$ relation. Figure 17b shows an example of the simulated sky. Among the simulated skies, we discarded ones with bright sources residing outside of the GIS f.o.v. ($r > 20\,{\rm mm} \simeq 20'$), with the same criterion in selecting the AMSS fields as indicated in figure 2. In order to imitate the source elimination, we further removed sources inside of the GIS f.o.v. ($r < 20\,{\rm mm} \simeq 20'$) if they were brighter than $S_0 = 2.0 \times 10^{-13}\,{\rm erg\,cm^{-2}\,s^{-1}}$ (2–10 keV). In the actual source elimination, finite regions surrounding these eliminated sources were also masked out, which reduced the averaged detection area by about 20%. On the other hand, 33 out of the 91 sample fields consisted of multi-pointing observations, covering a larger sky area than that with a single pointing ($0.40\,{\rm deg^2}$). As a result, the sky area covered by one sample field after source elimination, i.e. the mean value of the "Area 2" column of table 1, is $0.44\,{\rm deg^2}$ on average, which is 10% larger than the integration area for a single pointing without any source elimination.

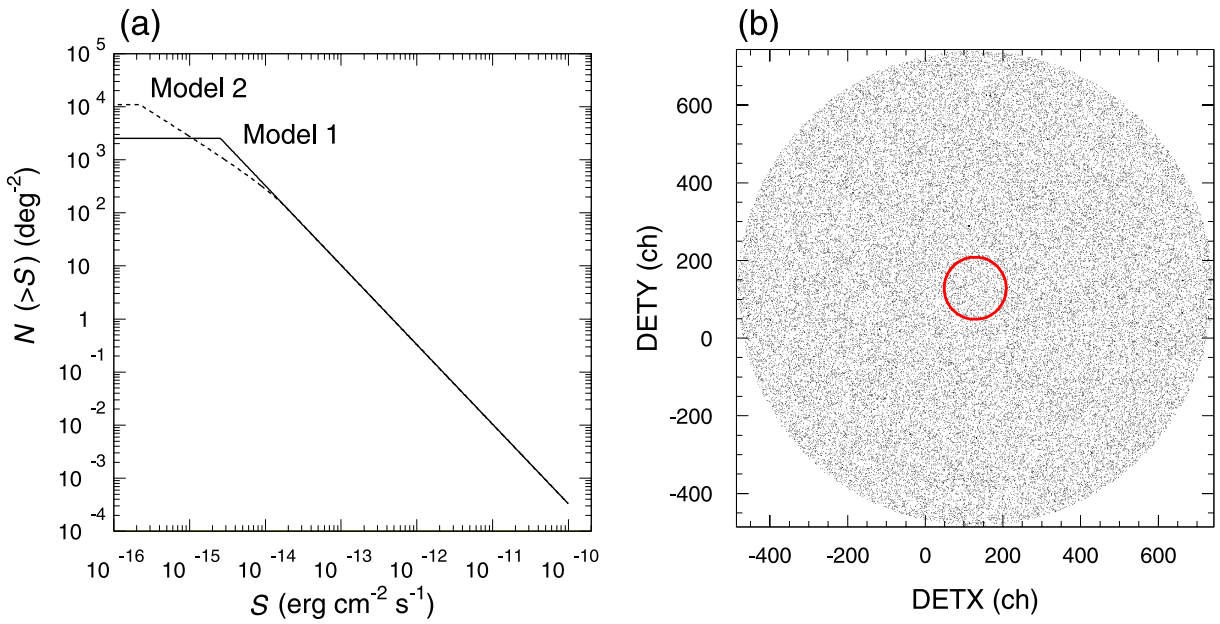

Fig. 17. Panel (a) shows two assumed $\log N - \log S$ curves. Model 1 is the nominal curve ($\gamma = 2.5$) compared with the observed data, and Model 2 includes the flattening in the low flux range ($S < 2 \times 10^{-14}\,\mathrm{erg\,cm^{-2}\,s^{-1}}$), as reported recently. Panel (b) shows the simulated sample image ($r < 2.^{\circ}5$) following the $\log N - \log S$ relation. The central circle represents the GIS field of view, $r = 20\,\mathrm{mm} \simeq 20'$.

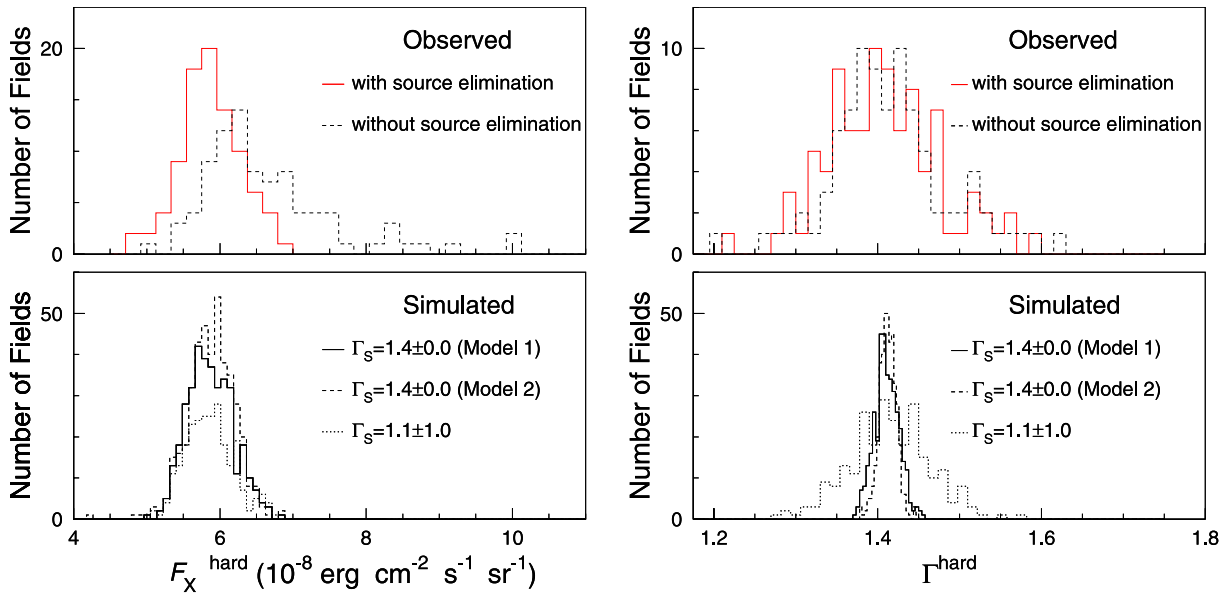

Fig. 18. Distribution of the 2–10 keV flux $F_{\mathrm{X}}^{\mathrm{hard}}$ (left panels) and the photon index Γ^{hard} (right panels). The upper panels represent the observed distributions, with solid and dotted histograms showing with and without the source elimination, respectively. The lower panels show simulation results. The solid and dotted lines are for a fixed energy spectrum ($\Gamma_{\mathrm{S}} = 1.4 \pm 0.0$) and for the Gaussian distribution ($\Gamma_{\mathrm{S}} = 1.1 \pm 1.0$), respectively. In both cases, the source elimination was applied.

Indeed, these finite sizes of the masking around bright sources or overlapping multipointing imply non-independent data. These effects, however, reconcile with a non-uniform exposure, as long as the source distribution is random, e.g. clustering of sources in a few arcmin scale can be neglected. We investigated this effect in the simulation by changing the integration area, S, on the detector. According to equation (11), a mild $S^{-0.5}$ dependence of the fluctuation width is expected. Five patterns of the integration area were tested; namely, we masked out a certain range of azimuth angles, like a pie cutting, with opening angles of 0°, 30°, 60°, 120°, and 180°. We found that differences in the following simulation results are small and within statistical errors between 0° (100% detector area) and 60° (83%) cases. Hence, we refer only to the results with a 100% detector area hereafter.

We lastly generated more than ten millions of photons for

each simulated sky following its intensity map in the energy range of 1–12 keV, while assuming that all of the sources have a common power-law energy spectrum with $\Gamma = 1.4$. The number of photons was chosen so that it would correspond to a 100 ks exposure with the GIS. We conducted a full instrumental simulation of the XRT and the GIS for each photon, which uses basically the same code with the SimARF, utilizing the ray-tracing and the standard response matrices of `gis2/3v4_0.rmf`. Photons detected by the GIS were collected to make an energy spectrum. Simulations with GIS 2 and GIS 3 were run separately for a sky, and the resultant two spectra were summed up afterwards. We performed this instrumental simulation for 369 simulated skies, and generated a set of spectra of the same number. Each spectrum was fit by a single power-law model in the 2–10 keV band, with a common response created by the SimARF in the same way as described in subsection 2.4, assuming a flat surface brightness. Note that the NXB was not taken into account in the simulation. The contribution of the NXB reproducibility is examined separately in the following subsection, so that we can evaluate the pure Poisson noise effect in the observed fluctuation.

5.3. Comparison of Results

We thus obtained 369 set of parameters, $F_{\rm X}^{\rm hard}$ and $\Gamma^{\rm hard}$, for the assumed $\log N - \log S$ relation. The distributions of $F_{\rm X}^{\rm hard}$ and $\Gamma^{\rm hard}$ for both the observation and the simulation are shown in figure 18. In the following comparison, we must take care that each parameter has an individual error of fitting, i.e. statistical error. We therefore calculated a weighted average, $\mathrm{A_v}(y)$, and its 1σ error, $\delta \mathrm{A_v}(y)$, for a parameter y as

$$\mathrm{A_v}(y) = \sum_i^{N_{\rm F}} \frac{y_i}{\sigma_i^2} \Big/ \sum_i^{N_{\rm F}} \frac{1}{\sigma_i^2}, \tag{7}$$

$$\delta \mathrm{A_v}(y) = \sqrt{\frac{1}{N_{\rm F}-1} \sum_i^{N_{\rm F}} \frac{[y_i - \mathrm{A_v}(y)]^2}{\sigma_i^2} \Big/ \sum_i^{N_{\rm F}} \frac{1}{\sigma_i^2}}, \tag{8}$$

where i, taking between 1 and $N_{\rm F}$, denotes the field ID of observations or simulations, and y_i and σ_i denote the best-fit value and its 1σ error, respectively. Intrinsic variance $\mathrm{Sd}^2(y)$ and its 1σ error $\delta \mathrm{Sd}^2(y)$, after subtracting the statistical error, were computed as

$$\mathrm{Sd}^2(y) = \sum_i^{N_{\rm F}} \frac{[y_i - \mathrm{A_v}(y)]^2}{\sigma_i^2} \Big/ \sum_i^{N_{\rm F}} \frac{1}{\sigma_i^2} - N_{\rm F} \Big/ \sum_i^{N_{\rm F}} \frac{1}{\sigma_i^2}, \tag{9}$$

$$\delta \mathrm{Sd}^2(y) = \sqrt{\frac{2}{N_{\rm F}-1} \sum_i^{N_{\rm F}} \frac{[y_i - \mathrm{A_v}(y)]^2}{\sigma_i^2} \Big/ \sum_i^{N_{\rm F}} \frac{1}{\sigma_i^2}}. \tag{10}$$

Equations (7)–(10) are correct as long as both the intrinsic distribution of the parameter y and the distribution of statistical error of y_i have Gaussian shapes. This assumption seems to be a good approximation for the parameters after source elimination, as can be seen in the left-hand panel of figure 18, although this is not true for those without the source elimination where the distribution of $F_{\rm X}^{\rm hard}$ has a non-symmetric shape.

With regard to the observed $F_{\rm X}^{\rm hard}$ after the source elimination, $\mathrm{A_v}(F_{\rm X}^{\rm hard})$ was calculated to be $(5.85 \pm 0.04) \times 10^{-8}\,\mathrm{erg\,cm^{-2}\,s^{-1}\,sr^{-1}}$ with a standard deviation of $\sqrt{\mathrm{Sd}^2(F_{\rm X}^{\rm hard})} = 0.38^{+0.03}_{-0.04} \times 10^{-8}\,\mathrm{erg\,cm^{-2}\,s^{-1}\,sr^{-1}}$, which corresponds to a $6.49^{+0.56}_{-0.61}\%$ fluctuation. From the simulation discussed in subsection 5.2, $\mathrm{A_v}(F_{\rm X}^{\rm hard})$ was obtained to be $(5.77 \pm 0.02) \times 10^{-8}\,\mathrm{erg\,cm^{-2}\,s^{-1}\,sr^{-1}}$ with a fluctuation width of $5.06^{+0.19}_{-0.20}\%$. These average values are in good agreement between the observation and the simulation, while the observed fluctuation is larger than that of the simulation. This discrepancy can be explained by the systematic error, mainly due to a NXB reproducibility of $\sim 3\%$. From table 3, the contribution of the systematic error to $F_{\rm X}^{\rm hard}$ is estimated to be $\sigma_{\rm S} = 3.2\%$. Then, the simulation becomes consistent with the observation at 1σ level, if considering the systematic error. Therefore, we can say that the Euclidean distribution of $\gamma = 2.5$ is acceptable with the present data.

As for the observed power-law photon index, $\mathrm{A_v}(\Gamma^{\rm hard})$ and $\sqrt{\mathrm{Sd}^2(\Gamma^{\rm hard})}$ were obtained to be 1.412 ± 0.007 and $0.055^{+0.005}_{-0.006}$, respectively, and $\mathrm{A_v}(\Gamma^{\rm hard}) = 1.414 \pm 0.001$ and $\sqrt{\mathrm{Sd}^2(\Gamma^{\rm hard})} = 0.009^{+0.001}_{-0.001}$ were calculated for the simulated results. The contribution of the systematic error to $\Gamma^{\rm hard}$ is estimated to be 0.025 from table 3. We have also examined a contribution due to the large-scale anisotropy using the dipole analysis, and it is estimated 0.011 ± 0.003 at most. Therefore, the observed distribution of $\Gamma^{\rm hard}$ is wider than that of the simulation, even though considering the systematic error and the large-scale anisotropy. This discrepancy is presumably due to the unrealistic assumption that all the sources have a common power-law index of $\Gamma = 1.4$ in the simulation. We investigate this effect later.

5.4. CXB Intensity

In order to determine the *correct* CXB intensity in a well-defined flux range, some compensation for the stray light is required, because the *ASCA* data has a significant flux contribution from outside of the f.o.v., where we cannot eliminate bright point sources. In the previous subsection, we showed that the assumed $\log N - \log S$ relation is in good agreement with the observed intensity and fluctuation of $F_{\rm X}^{\rm hard}$. We therefore calculated the *correct* CXB intensity using the assumed $\log N - \log S$ relation.

Spectral fits for the simulated data indicate that $F_{\rm X}^{\rm hard} = (5.77 \pm 0.02) \times 10^{-8}\,\mathrm{erg\,cm^{-2}\,s^{-1}\,sr^{-1}}$. Meanwhile, a simple integration of the assumed $\log N - \log S$ relation, i.e. equation (6), gives $F(S_0) = F_0 = 5.59 \times 10^{-8}\,\mathrm{erg\,cm^{-2}\,s^{-1}\,sr^{-1}}$ in the flux range $S < S_0 = 2.0 \times 10^{-13}\,\mathrm{erg\,cm^{-2}\,s^{-1}}$ (2–10 keV). This is 3.2% less than the simulation value which includes the contribution of bright discrete sources residing outside of the f.o.v. by chance. If we integrate this $\log N - \log S$ curve to $S \to \infty$, $F(\infty)$ becomes $6.29 \times 10^{-8}\,\mathrm{erg\,cm^{-2}\,s^{-1}\,sr^{-1}}$ (2–10 keV) which is 9.0% larger than the simulated value. Therefore, the compensation factor is -3.2% in the flux range $S < S_0$ and $+9.0\%$ for the total CXB flux, respectively. These compensation factors do not change, even though the $\log N - \log S$ relation has a break in the flux range of $S < S_0$, as long as the $\log N - \log S$ has the same shape at $S > S_0$, where we think the Euclidean slope of $\gamma = 2.5$ has been almost established. This is because the sources affecting the compensation factor have fluxes brighter

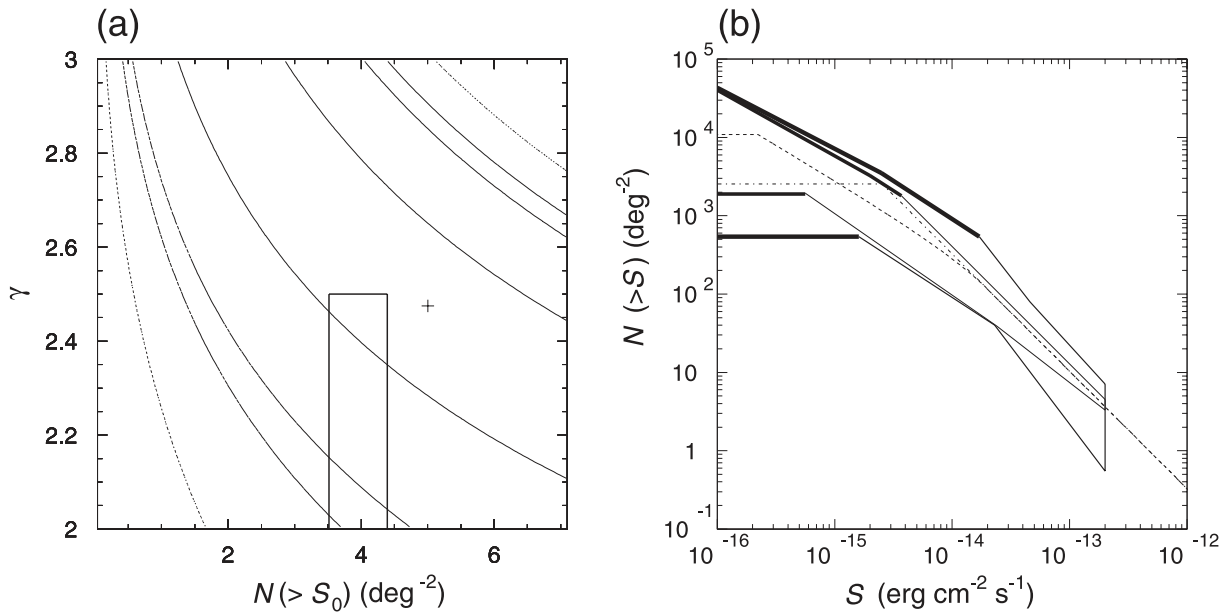

Fig. 19. In panel (a), the curves indicate the acceptable range in the $N(>S_0)$ versus γ plane. The contours correspond to $\Delta\chi^2 = 1.0$ (68.3%), 4.61 (90%), 5.99 (95%), and 9.21 (99% confidence range), respectively. The best-fit point is shown by a cross. The square region shows the constraint derived from other studies: $\gamma < 2.5$ is given by recent *Chandra* and *XMM-Newton* observations (e.g. Baldi et al. 2002; Tozzi et al. 2001), and $N(>S_0) = 3.95 \pm 0.43\,\mathrm{deg}^{-2}$ is estimated from the previous AMSS study (Ueda et al. 1999b). Panel (b) shows the $\log N - \log S$ relation matching the acceptable $N(>S_0)$ and γ values with two models (dotted lines). The outer solid lines correspond to the 90% confidence limits in panel (a), and the inner solid lines include the additional constraint by the square region in (a). In both the outer and the inner lines, the thick ones are boundaries, where the $\log N - \log S$ curves crosses the 100 % CXB flux, which we determined in section 5.

than S_0, which by chance lie outside of the f.o.v.

By applying the compensation factor to the observed CXB intensity, the unresolved CXB flux from sources fainter than S_0 were reduced to $(5.67 \pm 0.04) \times 10^{-8}\,\mathrm{erg\,cm^{-2}\,s^{-1}\,sr^{-1}}$ (2–10 keV) when averaged for the 91 sample fields and corrected for the Galactic absorption. On the other hand, the total CXB flux integrated over $S \to \infty$ was calculated to be $(6.38 \pm 0.04) \times 10^{-8}\,\mathrm{erg\,cm^{-2}\,s^{-1}\,sr^{-1}}$. Note that this value does not include the soft component, and that the absolute flux determined with *ASCA* has a systematic error of about 10%, when compared with the recent results of *Chandra* or *XMM-Newton*. If we convert the latter intensity into a power-law normalization at 1 keV, assuming a photon index of $\Gamma = 1.4$, we obtain $9.66 \pm 0.07\,\mathrm{photon\,keV^{-1}\,cm^{-2}\,s^{-1}\,sr^{-1}}$, which is entirely consistent with a calculation by Barcons et al. (2000) of $10.0^{+0.6}_{-0.9}\,\mathrm{photon\,keV^{-1}\,cm^{-2}\,s^{-1}\,sr^{-1}}$ (90% confidence errors) using the *ASCA* and *BeppoSAX* results. Though this representation is conventionally used in much CXB literature, this value is very susceptible to the existence of the soft component and the power-law index of the hard component. For example, changing the power-law index, Γ, by only 0.01 causes a shift of normalization at 1 keV by as much as 16%.

5.5. *Constraint on the log N–log S Relation*

We then tried to constrain the acceptable range of the $\log N - \log S$ relation based on the analytic dependence of the fluctuation width for a given set of (k, γ). The $S_{\min}$ value was determined for each (k, γ) pair, using equation (6) with $F(S_0) = 5.67 \times 10^{-8}\,\mathrm{erg\,cm^{-2}\,s^{-1}\,sr^{-1}}$ (2–10 keV). According to Condon (1974), the fluctuation width σ_{F} is given analytically as

$$\sigma_{\mathrm{F}} \equiv \frac{\sqrt{\mathrm{Sd}^2}}{\mathrm{A_v}} = \frac{\gamma - 2}{S_{\min}^{-\gamma+2} - S_0^{-\gamma+2}} \sqrt{\frac{S_0^{3-\gamma} - S_{\min}^{3-\gamma}}{(3-\gamma) k \Omega_{\mathrm{eff}}}}, \tag{11}$$

where Ω_{eff} represents the effective beam size of the XRT + GIS system. If we take the values derived from the simulation, i.e. $\sigma_{\mathrm{F}} = 5.06\%$, etc., Ω_{eff} is calculated to be $0.516\,\mathrm{deg}^2$. Using this Ω_{eff} value and given (k, γ) pair, we calculated equation (11) and searched for an acceptable range in the (k, γ) plane. In the parameter search, we defined $\chi^2(\sigma_{\mathrm{F}})$ as

$$\chi^2(\sigma_{\mathrm{F}}) \equiv \left[\frac{\mathrm{Sd}^2 - (\sigma_{\mathrm{F}} \cdot \mathrm{A_v})^2 - (\sigma_{\mathrm{S}} \cdot \mathrm{A_v})^2}{\delta \mathrm{Sd}^2 + \sqrt{\frac{2}{N_{\mathrm{F}} - 1} (\sigma_{\mathrm{S}} \cdot \mathrm{A_v})^2}} \right]^2, \tag{12}$$

where σ_{S} denotes the systematic error of 3.2%.

Since the χ^2 value is determined by γ and k, namely, the degree of freedom equals two, the 90% confidence range of σ_{F} can be evaluated as $\chi^2(\sigma_{\mathrm{F}}) < 4.61$. In figure 19a, we plot the region where the (k, γ) pair gives the 90% confidence range of σ_{F}, as well as that of 68.3%, 95%, and 99%. In this plot, we converted k into $N(>S_0)$, which represents the $N(>S)$ value for given (k, γ) at $S = S_0 = 2 \times 10^{-13}\,\mathrm{erg\,cm^{-2}\,s^{-1}}$. The resultant 90% acceptable region of the $\log N - \log S$ relation is shown in figure 19b by the outer solid lines. Roughly speaking, this region is constrained by two factors. One is a constraint by the fluctuation, which is expressed by the thin solid lines. The other is a constraint by the absolute CXB intensity shown by the thick solid lines, where the integrated source flux reaches 100% of the absolute CXB intensity, when the power-law-like

Table 4. Simulation results on the fluctuation width compared with the analytical formula.

k	γ	$S_{\rm min}$ (erg cm^{-2} s^{-1})	$N(>S_0)$ (deg^{-2})	$\sigma_{\rm F}$	Fluctuation	$N_{\rm F}$
1.98×10^{-14}	2.42	1.77×10^{-15}	3.99	5.04%	$4.78^{+0.37}_{-0.40}$%	83
1.58×10^{-15}	2.50	2.52×10^{-15}	3.59	5.06%	$5.06^{+0.19}_{-0.20}$%	369
1.00×10^{-19}	2.82	6.10×10^{-15}	2.44	5.26%	$5.97^{+0.45}_{-0.49}$%	79

Note. Errors in the fluctuation are 1σ.

log N–log S relation is extrapolated towards the fainter flux range. In practice, the constraint by the fluctuation is valid only in the brighter flux range where the Poisson noise, $\sqrt{N}$, of the source count, N, in the f.o.v. is comparable to the fluctuation width, i.e., $N(>S)\lesssim 50$ with our data. On the other hand, the log N–log S relation must be within the range of the constraint by the absolute CXB intensity, as long as the log N–log S curve has a form that is gradually flattening.

Although our obtained region is fairly wide, we can further constrain the region by rejecting an unrealistic set of (k,γ) which contradict with the previous results. When combined with the LSS and the AMSS results (Ueda et al. 1999a and b, respectively), $N(>S)$ value at $S=S_0$ is determined in the range of $3.52\,{\rm deg}^{-2} < N\,(>S_0) < 4.38\,{\rm deg}^{-2}$. Recent deep observations with *Chandra* and *XMM-Newton* show that the flattening of the log N–log S curve comes out at a fainter flux around $(1\text{–}2)\times10^{-14}\,{\rm erg\,cm^{-2}\,s^{-1}}$ (e.g. Baldi et al. 2002; Tozzi et al. 2001). Hence, we made another condition of $\gamma\le 2.5$. If these two conditions are added, the acceptable region of the (k,γ) pair becomes the area surrounded by a rectangle, as shown in figure 19a, and the acceptable log N–log S region becomes the area surrounded by the inner solid lines in figure 19b. Therefore, the log N–log S relation would reach 100% of the CXB at $S<3.7\times10^{-15}\,{\rm erg\,cm^{-2}\,s^{-1}}$ if there were no flattening, and the source density at $S=10^{-16}\,{\rm erg\,cm^{-2}\,s^{-1}}$ is in the range of 1900–40000 deg^{-2}.

As a confirmation, we tried a simulation while assuming a bending log N–log S curve, as shown in figures 17 and 19b (Model 2). The model was acceptable with a fluctuation width of $5.48^{+0.19}_{-0.20}$%. We also confirmed the consistency with the analytic formula, equation (11), by running simulations for the boundary values of k and γ. These results are summarized in table 4.

5.6. *Spectral Distribution of Sources*

As described in subsection 5.3, the simulation could not reproduce the observed deviation of the CXB spectral index, Γ, whereas both the average value and the deviation of $F_{\rm X}^{\rm hard}$ were explained by the simulation fairly well. This is partly due to the assumption that all of the sources had a common spectral index of $\Gamma=1.4$ in the simulation. We therefore investigated the dependence of the apparent CXB spectral index upon the intrinsic distribution of the source spectra.

In order to investigate this effect, we introduced a Gaussian distribution of power-law index $\Gamma_{\rm S}$ for those sources which constitute the CXB. We assumed that the distribution of the source spectra is independent of the source flux. We chose these assumptions for simplicity, although the actual Universe is much more complex. For instance, hardening of source spectra towards fainter flux range has already been seen in the AMSS survey (Ueda et al. 1999b), and the hard sources are usually heavily absorbed sources; hence, sources with intrinsically flat spectral indices are rare. However, modeling all of these characteristics is beyond our scope.

Table 5. Simulation results on $\Gamma^{\rm hard}$ compared with the observation.

$\Gamma_{\rm S}$	$A_{\rm v}(\Gamma^{\rm hard})$	$\sqrt{{\rm Sd}^2(\Gamma^{\rm hard})}$	$N_{\rm F}$
1.4 ± 0.0	1.414 ± 0.001	$0.009^{+0.001}_{-0.001}$	369
1.2 ± 0.5	1.397 ± 0.001	$0.020^{+0.001}_{-0.001}$	369
1.1 ± 1.0	1.422 ± 0.003	$0.031^{+0.003}_{-0.003}$	249
Observation	1.412 ± 0.007	$0.055^{+0.005}_{-0.006}$	91

Note. Errors are 1σ.

The simulation results for several $\Gamma_{\rm S}$ are summarized in table 5 along with the observed ones. The simulation suggests that the intrinsic deviation of the power-law index, Γ, is more than 1.0, even when considering the deviation due to the systematic error of the NXB which is estimated to be $\sqrt{{\rm Sd}^2(\Gamma^{\rm hard})}=0.025$ and the deviation due to the large-scale anisotropy of 0.011 ± 0.003. The intrinsic source spectra must peak at significantly harder index of $\Gamma_{\rm S}=1.1$ than the observed CXB index of $\Gamma^{\rm hard}\simeq1.4$ if we suppose that their spectral deviation is about 1.0. This is because sources with soft spectra emit more photons than do hard sources when they have the same flux; consequently, the averaged spectrum tends to be weighted towards the soft source. On the other hand, we also found that it was difficult to fit the simulated spectrum with a single power-law model for a larger deviation of $\Gamma_{\rm S}$, since the integrated spectrum became a concave shape. These funny effects are in part caused by the simplistic model, which is discussed in subsection 6.4.

6. Discussion

The present *ASCA* observations have shown interesting features in the large-scale distribution of the CXB. Below, we will summarize the main results and address their implications for each subject.

6.1. *CXB Intensity and Energy Spectrum*

As shown in section 3, the integrated energy spectrum of the 2–10 keV CXB after the source elimination for the total of 4.2 Ms exposure is described by a power-law model with a

photon index of $\Gamma^{\rm hard} = 1.411 \pm 0.007 \pm 0.025$ (errors at 90% statistical and systematic). The slope is consistent with many previous measurements. When the nominal NXB is subtracted, the residual from the power-law model suggests a systematic deviation above 8 keV as if the observed spectrum has the cut-off as shown in figure 10. However, this feature disappears when the NXB level is reduced by 3% within the systematic error. Therefore, we regard that the cut-off feature above 8 keV is not significant. Similarly, because the other residual features are all within the NXB uncertainty, we conclude that the energy spectrum of the CXB is consistent with the nominal power-law model in the energy range 2–10 keV.

The intensity of the power-law component was calculated to be 8.61 ± 0.07 photon keV^{-1} cm^{-2} s^{-1} sr^{-1} at 1 keV after eliminating sources with a flux greater than $S = 2 \times 10^{-13}$ erg cm^{-2} s^{-1}. If all the sources brighter than 2×10^{-13} erg cm^{-2} s^{-1} were included, the intensity would become 9.66 ± 0.07 photon keV^{-1} cm^{-2} s^{-1} sr^{-1} at 1 keV, using the compensation factor calculated in subsection 5.4. This value is consistent with the *ASCA* SIS result based on a 250 ks exposure in 4 fields, i.e. 9.4 ± 0.4 photon keV^{-1} cm^{-2} s^{-1} sr^{-1} (Gendreau et al. 1995). Note that these absolute fluxes with *ASCA* have systematic errors of $\sim 10\%$ because of the calibration uncertainty. Nevertheless, our result is considered to be the best estimate of the CXB intensity so far from two points of view: a well-calibrated and low-background instrument is used, and the source elimination ($S_0 \sim 2 \times 10^{-13}$ erg cm^{-2} s^{-1}) and large solid angle ($\Omega_{\rm eff} \sim 50$ deg^2) make the cosmic variance small enough, as expressed in equation (11). Compared with results from other missions, the present one is consistent with the *BeppoSAX* LECS value based on a two thermal plus a power-law model fit; $10.4^{+1.4}_{-1.1}$ photon keV^{-1} cm^{-2} s^{-1} sr^{-1} at 1 keV (Parmar et al. 1999). However, these values are much smaller than the *ROSAT* level of 13.4 ± 0.3 photon keV^{-1} cm^{-2} s^{-1} sr^{-1} at 1 keV (Hasinger 1992), even if we include the systematic error in the *ASCA* data. The relatively strong *ROSAT* flux is caused by the steeper spectrum with $\Gamma \sim 2.1$, which would be due to contamination of the soft component or the calibration differences (Barcons et al. 2000).

6.2. *The Galactic Component*

We found that the (l, b) profiles of both $F_{\rm X}^{\rm soft}$ and $F_{\rm X}^{\rm hard}$ can be fitted with acceptable χ^2 values by the finite radius disk model, which strongly suggests that a certain fraction of the X-ray emission has the Galactic origin. As for the soft thermal component ($F_{\rm X}^{\rm soft}$), all of the emission is consistent to be Galactic, with a scale height of $h = 1.5 \pm 0.6$ kpc and a disk radius of $R_{\rm d} = 9.2 \pm 1.8$ kpc (errors are 1σ), if we assume the distance to the Galactic Center to be $R_{\rm g} = 8$ kpc. The volume emissivity, $\eta(z_{\rm g})$, is expressed by

$$\eta(z_{\rm g}) = \frac{4\pi E}{h} \exp\left(-\frac{|z_{\rm g}|}{h}\right), \tag{13}$$

where $z_{\rm g}$ is the height above the plane. We can compute the total luminosity of the soft component by integrating $\eta(z_{\rm g})$ as

$$L_{\rm X} = \int_{-\infty}^{\infty} \eta(z_{\rm g})\, dz_{\rm g} \int_0^{R_{\rm d}} 2\pi r\, dr = 2(4\pi E)(\pi R_{\rm d}^2). \tag{14}$$

Hence, $L_{\rm X}^{\rm soft} = (1.2 \pm 0.7) \times 10^{39}$ erg s^{-1} (0.5–2 keV). Snowden et al. (1997) derived the total luminosity to be $\sim 2 \times 10^{39}$ erg s^{-1} from the *ROSAT* all-sky survey, which is consistent with our result. Note that the absolute value of $F_{\rm X}^{\rm soft}$ is very sensitive to the kT value, which does vary between 0.14 and 0.7 keV, bringing in a systematic error by about an order of magnitude in $L_{\rm X}^{\rm soft}$. Assuming the MEKAL model of the temperature $kT = 0.4$ keV and the metal abundance at one solar, the electron density in the Galactic plane is calculated as $n_{\rm e} = (1.5 \pm 0.5) \times 10^{-3}$ cm^{-3}.

In the same way, the Galactic component in the hard band ($F_{\rm X}^{\rm hard}$) is calculated as $L_{\rm X}^{\rm hard} \sim 8 \times 10^{38}$ erg s^{-1} (2–10 keV), although its detection is marginal. The $F_{\rm X}^{\rm hard}$ also showed a weak dipole feature with an amplitude of $3.0 \pm 1.6\%$ and the peak position near the Galactic Center, even though the pointed fields all lie above $|b| = 10°$. This result remained essentially the same when we simply took the count-rate data above 3 keV instead of the $F_{\rm X}^{\rm hard}$ obtained from the spectral fit. The soft component can be approximated by a thermal model with $kT \sim 0.4$ keV, and even if we take the highest value of $F_{\rm X}^{\rm soft}$ detected in the IRAS 19254−7245 field, the flux contribution above 3 keV is only $\sim 0.02\%$. This suggests that the distribution of the 2–10 keV X-rays in our Galaxy really has a high scale-height component. Essentially the same results were previously reported by Warwick et al. (1980) and Iwan et al. (1982) with the *Ariel V* and *HEAO 1* A-2 all-sky surveys, respectively.

Kokubun (2001) recently examined the spatial distribution of the so-called Galactic bulge and the ridge X-ray emission, which has a broad enhancement around the Galactic Center and plane, and showed that the spectrum can be described by a mixture of two thermal components (~ 0.6 keV and ~ 3 keV, respectively) and a non-thermal power-law component ($\Gamma \sim 1.8$). Based on an analysis of the *ASCA* and *RXTE* data, he suggested the typical scale-height/length of the bulge emission to be $b \sim 2°$ and $l \sim 7°$. A comparison with the present result implies that this emission is extending further away ($|b| > 10°$) from the Galactic Center with low surface brightness. Ebisawa et al. (2001) conducted a deep X-ray survey of a region in the Galactic plane with *Chandra* ACIS-I, and found that the hard X-ray emission from the Galactic ridge is truly diffuse, not resolved into discrete sources. However, there are difficulties in confining plasmas with such a energy density and temperature in the Galactic disk. The far extended hard X-ray emission in our data may indicate an escape of the high energy plasmas. The spatial distribution determined by the *ROSAT* all-sky survey gives $h \sim 0.95$ kpc[1] and $R_{\rm d} \sim 5.6$ kpc, which are slightly smaller than our results for the $F_{\rm X}^{\rm soft}$. This is possibly because the *ROSAT* PSPC is sensitive in a softer band than the *ASCA* GIS.

6.3. *log N–log S Relation*

Based on the observed fluctuation and the absolute intensity of the 2–10 keV CXB flux compared with the simulation results, the acceptable $\log N - \log S$ relation was constrained as shown in figure 20. In the flux range above $\sim 10^{-14}$ erg cm^{-2} s^{-1}, the relation follows the uniform Euclidean relation of $dN(>S)/dS \propto S^{-2.5}$, as already indicated from

[1] In Snowden et al. (1997), the scale height parameter is used for the gas density, hence we have multiplied their scale height by 0.5.

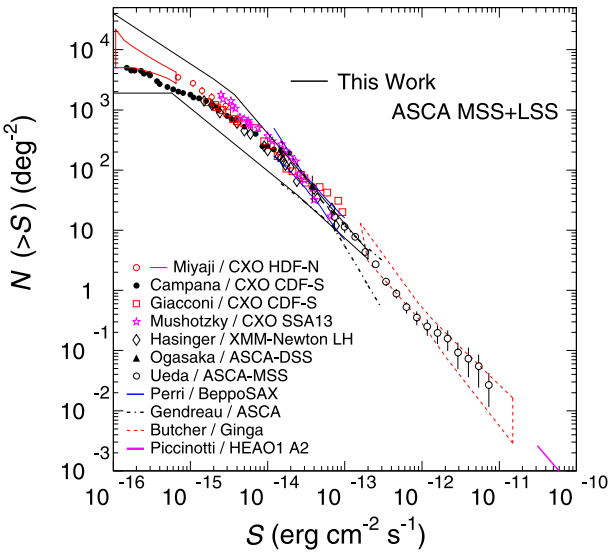

Fig. 20. $\log N - \log S$ relation in the energy range 2–10 keV constrained from the present study (thick solid line), compared with a number of previous results. The references compiled in this plot are Miyaji and Griffiths (2002), Campana et al. (2001), Giacconi et al. (2001), Mushotzky et al. (2000), Hasinger et al. (2001), Ogasaka et al. (1998), Ueda et al. (1999b), Perri and Giommi (2000), Gendreau et al. (1998), Butcher et al. (1997), and Piccinotti et al. (1982).

the previous observations, and lies on a fainter extension from the previous results from *Ginga* LAC (Butcher et al. 1997) and *HEAO 1* A-2 (Piccinotti et al. 1982). As figure 20 clearly shows, the present 90% confidence range of the $\log N - \log S$ curve is also consistent with the fainter-part results obtained from the recent *Chandra* and *XMM-Newton* deep-survey observations. We cannot say where the turn-over exactly occurs, but it is close to the 10^{-15}–$10^{-14}\,\mathrm{erg\,cm^{-2}\,s^{-1}}$ level from the derived envelope of figure 20. Miyaji and Griffiths (2002) recently analyzed *Chandra* data for the Hubble Deep Field North with an area of 35.7 arcmin^2 by the fluctuation method. They derived a loose upper limit in the number density at the flux level of $2 \times 10^{-16}\,\mathrm{erg\,cm^{-2}\,s^{-1}}$ in the 2–10 keV band to be less than 10000 per square degree. As figure 20 shows, the present *ASCA* result in the same energy band gives a consistent upper limit of ~ 22000 per square degree, in the sense that an extrapolation of the $\log N - \log S$ curve reaches 100% of the CXB intensity at this point.

The recent *Chandra* results also suggest an $\sim 8\%$ difference in the source contribution brighter than $S > 4.5 \times 10^{-16}\,\mathrm{erg\,cm^{-2}\,s^{-1}}$ between the CDF-N and the CDF-S fields (Rosati et al. 2002). However, the measured intensity, i.e. $(5.58 \pm 0.56) \times 10^{-8}\,\mathrm{erg\,cm^{-2}\,s^{-1}}$ (CDF-N) and $(5.15 \pm 0.49) \times 10^{-8}\,\mathrm{erg\,cm^{-2}\,s^{-1}}$ (CDF-S) in 2–10 keV, have fairly large errors of $\sim 10\%$, and both fields are restricted to relatively small areas ($\simeq 0.1\,\mathrm{deg^2}$). As pointed out by Barcons et al. (2000), the cosmic variance plays an important role in such small-area observations. We have shown in section 5 that $\sim 5\%$ of the intensity deviation can be reproduced even by a single $\log N - \log S$ relation, and that the fluctuation width is inversely proportional to the square root of the observed area, i.e. $\sigma_\mathrm{F} \propto 1/\sqrt{\Omega_\mathrm{eff}}$ from equation (11). Considering that the GIS + XRT effective beam-size, Ω_eff, is about $0.5\,\mathrm{deg^2}$, it is not unusual that the intensities of the CDF-N and the CDF-S differ by $\sim 8\%$. If we take our average value of the CXB intensity integrated up to $S \to \infty$, i.e. $(6.38 \pm 0.04) \times 10^{-8}\,\mathrm{erg\,cm^{-2}\,s^{-1}\,sr^{-1}}$, the fraction of CXB resolved into discrete sources can be $80.8 \pm 7.7\%$ in CDF-S and $87.5 \pm 8.8\%$ in CDF-N, respectively, although these values do not take into account the uncertainty ($\sim 10\%$) of the absolute flux with *ASCA*.

6.4. *Spectral Fluctuation*

As shown in subsection 5.3, the observed distribution of Γ^hard indicates $1\,\sigma = 0.055^{+0.005}_{-0.006}$. If we try to explain this in terms of the Gaussian distribution of the spectral index of discrete sources, we need to set the intrinsic fluctuation width to be larger than 1.0 ($1\,\sigma$), and a significant fraction of the sources must have a harder spectrum than the CXB with an average of $\Gamma_\mathrm{S} \sim 1.1$. This suggests a possibility that faint sources do not distribute along a simple $\log N - \log S$ relation, but may consist of two or more different populations. However, the present spectral fluctuation may be partly coupled with the Galactic structure which affects the observed variation of Γ^hard by $\sim 0.011 \pm 0.003$ at the maximum. Also, the systematic error on the index caused by the NXB subtraction is 0.025. The simulated fluctuation of Γ^hard is ± 0.031 for a single $\log N - \log S$ curve with an intrinsic $\Gamma_\mathrm{S} = 1.1 \pm 1.0$; therefore, the total fluctuation, including the NXB effect, amounts to 0.041 and approaches the observed level.

We also note that the Gaussian approximation for the distribution of the spectral index is not adequate. The actual situation may be that the distribution broadly consists of two components: one corresponds the population of unabsorbed AGNs with the peak of index distribution around $\Gamma_\mathrm{S} \simeq 1.7$, and the other contains heavily absorbed galaxies with their absorption ranging over a widely different levels. In fact, several models have been proposed along with this picture, e.g. by Madau et al. (1994), Comastri et al. (1995), and Gilli et al. (2001), and they were successful in explaining the spectral shape of the CXB. However, the distributions of the intrinsic absorption of AGN in these models are based on some assumptions and/or limited observations of nearby AGNs (e.g. 45 Seyferts of $z < 0.025$ in Risaliti et al. 1999). Because of the observed spectral fluctuation in our result should include all of the contribution from faint distant AGNs, it remains to be studied whether these models can also reproduce the spectral fluctuation with $1\,\sigma \simeq 0.05$ when observed with a solid angle of $\Omega_\mathrm{eff} \simeq 0.5\,\mathrm{deg^2}$.

7. Conclusion

We measured the absolute CXB intensity and its spectrum from 50 square degrees based on the low background data with the *ASCA* GIS instrument. A total of 91 selected fields were studied after eliminating discrete sources with a threshold of $\sim 2 \times 10^{-13}\,\mathrm{erg\,cm^{-2}\,s^{-1}}$ (2–10 keV). The energy spectrum in the energy range of 0.7–10 keV is well described by a two-component model comprizing a soft thermal emission with $kT \simeq 0.4$ keV and a hard power-law model with photon index $\Gamma^\mathrm{hard} = 1.412 \pm 0.007 \pm 0.025$ ($1\,\sigma$ statistical and systematic errors). As for the extragalactic power-law emission, the

intensity fluctuation is $1\sigma = 6.49^{+0.56}_{-0.61}\%$, while the deviation due to the reproducibility of the NXB is 3.2%. We also observed a fluctuation in the photon index of $0.055^{+0.005}_{-0.006}$, with a NXB contribution of 0.025.

We detected an excess emission toward the Galactic Center in both the soft (0.7–2 keV) and hard (2–10 keV) energy bands, which could be fitted by a finite radius disk model. The emission extends well above $|b| = 10^\circ$. The soft thermal component is consistent to be totally Galactic, whereas, for the hard power-law component in the 2–10 keV band, the contribution form the Galaxy is 3–7%. The soft component showed a strong correlation with the RASS map in the 3/4 keV and 1.5 keV bands.

To understand the intrinsic properties of the CXB emission, we carried out a simulation including the stray-light effect. We found the absolute CXB intensity to be $(6.38 \pm 0.04 \pm 0.64) \times 10^{-8}\,\mathrm{erg\,cm^{-2}\,s^{-1}\,sr^{-1}}$ (1σ statistical and systematic errors) in the 2–10 keV band. The observed fluctuation can be explained by the Poisson noise of the source count in the f.o.v. ($\Omega_{\mathrm{eff}} \simeq 0.5\,\mathrm{deg}^2$), even assuming a single $\log N - \log S$ relation on the whole sky. Based on the observed fluctuation and the absolute intensity, an acceptable region of the $\log N - \log S$ relation was derived, and the source density at $S = 10^{-16}\,\mathrm{erg\,cm^{-2}\,s^{-1}}$ is constrained in the range of 1900–40000 deg^{-2}. The results turned out to be consistent with previous measurements including the recent *Chandra* and *XMM-Newton* results. The spectral fluctuation was modeled with a Gaussian distribution of photon index, and the simulation indicated that the intrinsic r.m.s. width of Γ is larger than 1.0 with a peak around $\Gamma = 1.1$, suggesting a large amount of hard sources and a large variation in the intrinsic source spectra.

The authors thank all of the *ASCA* team members for their developing hardware and software, spacecraft operations, and instrumental calibrations. We especially appreciate the ASCA_ANL and the SimASCA teams for support in building the data analysis tools. We are grateful to Dr. K. Kikuchi and Mr. T. Kagei for help on making the NXB database. We also wish to thank Dr. K. Hayashida, Dr. K. Masai, and the referee Dr. X. Barcons for their useful comments and suggestions to improve this manuscript. This work is supported in part by Grant-in-Aid for Scientific Research (No. 12304009) from the Japan Society for the Promotion of Science.

References

Akiyama, M., Ohta, K., Yamada, T., Kashikawa, N., Yagi, M., Kawasaki, W., Sakano, M., Tsuru, T., et al. 2000, ApJ, 532, 700
Arnaud, K. 1996, in ASP Conf. Ser. 101, Astronomical Data Analysis Software and Systems V, ed. G. H. Jacoby & J. Barnes (San Francisco: ASP), 17
Baldi, A., Molendi, S., Comastri, A., Fiore, F., Matt, G., & Vignali, C. 2002, AJ, 564, 190
Barcons, X., Mateos, S., & Ceballos, M. T. 2000, MNRAS, 316, L13
Bowyer, C. S., Field, G. B., & Mack, J. E. 1968, Nature, 217, 32
Brandt, W. N., Hornschemeier, A. E., Alexander, D. M., Garmire, G. P., Schneider, D. P., Broos, P. S., Townsley, L. K., Bautz, M. W., Feigelson, E. D., & Griffiths, R. E. 2001, AJ, 122, 1
Butcher, J. A., Stewart, G. C., Warwick, R. S., Fabian, A. C., Carrera, F. J., Barcons, X., Hayashida, K., Inoue, H., & Kii, T. 1997, MNRAS, 291, 437
Campana, S., Moretti, A., Lazzati, D., & Tagliaferri, G. 2001, ApJ, 560, L19
Comastri, A., Setti, G., Zamorani, G., & Hasinger, G. 1995, A&A, 296, 1
Condon, J. J. 1974, ApJ, 188, 279
Dickey, J. M., & Lockman, F. J. 1990, ARA&A, 28, 215
Ebisawa, K., Maeda, Y., Kaneda, H., Yamauchi, S. 2001, Science, 293, 1633
Fabian, A. C., & Barcons, X. 1992, ARA&A, 30, 429
Fukazawa, Y., Ishida, M., & Ebisawa, K. 1997, ASCA News, 5, 3, available on the WWW at ⟨http://heasarc.gsfc.nasa.gov/docs/asca/newsletters/crab_calibrations5.html⟩
Gendreau, K. C., Barcons, X., & Fabian, A. C. 1998, MNRAS, 297, 41
Gendreau, K. C., Mushotzky, R., Fabian, A. C., Holt, S. S., Kii, T., Serlemitsos, P. J., Ogasaka, Y., Tanaka, Y., et al. 1995, PASJ, 47, L5
Giacconi, R., Gursky, H., Paolini, F. R., & Rossi, B. B. 1962, Phys. Rev. Lett., 9, 439
Giacconi, R., Rosati, P., Tozzi, P., Nonino, M., Hasinger, G., Norman, C., Bergeron, J., Borgani, S., et al. 2001, ApJ, 551, 624
Gilli, R., Salvati, M., & Hasinger, G. 2001, A&A, 366, 407
Hasinger, G. 1992, in The X-Ray Background, ed. X. Barcons & A. C. Fabian (Cambridge: Cambridge University Press), 229
Hasinger, G., Altieri, B., Arnaud, M., Barcons, X., Bergeron, J., Brunner, H., Dadina, M., Dennerl, K., et al. 2001, A&A, 365, L45
Hayashida, K., Inoue, H., & Kii, T. 1992, in Frontiers of X-Ray Astronomy, ed. Y. Tanaka & K. Koyama (Tokyo: Universal Academy Press), 653
Honda, H., Hirayama, M., Watanabe, M., Kunieda, H., Tawara, Y., Yamashita, K., Ohashi, T., Hughes, J. P., & Henry, J. P. 1996, ApJ, 473, L71
Ikebe, Y., Makishima, K., Ezawa, H., Fukazawa, Y., Hirayama, M., Honda, H., Ishisaki, Y., Kikuchi, K., et al. 1997, ApJ, 481, 660
Ishisaki, Y. 1996, PhD Thesis, The University of Tokyo, available on the WWW at ⟨http://www.astro.isas.ac.jp/asca/bibliography/phd_thesis.html⟩
Ishisaki, Y., Ueda, Y., Kubo, H., Ikebe, Y., Makishima, K., & the GIS team 1997, ASCA News, 5, 26, available on the WWW at ⟨http://heasarc.gsfc.nasa.gov/docs/asca/newsletters/gis_reproducibility5.html⟩
Ishisaki, Y., Ueda, Y., Yamashita, A., Ohashi, T., Lehmann, I., & Hasinger, G. 2001, PASJ, 53, 445
Iwan, D., Marshall, F. E., Boldt, E. A., Mushotzky, R. F., Shafer, R. A., & Stottlemyer, A. 1982, ApJ, 260, 111
Jahoda, K., Serlemitsos, P. J., Arnaud, K. A., Boldt, E., Holt, S., Marshall, F. E., Mushotzky, R. F., Petre, R., et al. 1992, in The X-Ray Background, ed. X. Barcons & A. C. Fabian (Cambridge: Cambridge University Press), 240
Kerp, J. 1994, A&A, 289, 597
Kokubun, M. 2001, PhD Thesis, The University of Tokyo
Liedahl, D. A., Osterheld, A. L., & Goldstein, W. H. 1995, ApJ, 438, L115
Lineweaver, C. H., Tenorio, L., Smoot, G. F., Keegstra, P., Banday, A. J., & Lubin, P. 1996, ApJ, 470, 38
Madau, P., Ghisellini, G., & Fabian, A. C. 1994, MNRAS, 270, L17
Makishima, K., Tashiro, M., Ebisawa, K., Ezawa, H., Fukazawa, Y., Gunji, S., Hirayama, M., Idesawa, E., et al. 1996, PASJ, 48, 171

Marshall, F. E., Boldt, E. A., Holt, S. S., Miller, R. B., Mushotzky, R. F., Rose, L. A., Rothschild, R. E., & Serlemitsos, P. J. 1980, ApJ, 235, 4
Mendenhall, J. A., & Burrows, D. N. 2001, ApJ, 563, 716
Miyaji, T., & Griffiths, R. E. 2002, ApJ, 564, L5
Miyaji, T., Ishisaki, Y., Ogasaka, Y., Ueda, Y., Freyberg, M. J., Hasinger, G., & Tanaka, Y. 1998, A&A, 334, L13
Mushotzky, R. F., Cowie, L. L., Barger, A. J., & Arnaud, K. A. 2000, Nature, 404, 459
Ogasaka, Y., Kii, T., Ueda, Y., Takahashi, T., Inoue, H., Ishisaki, Y., Ohta, K., Yamada, T., et al. 1998, Astron. Nachr., 319, 43
Ohashi, T., Ebisawa, K., Fukazawa, Y., Hiyoshi, K., Horii, M., Ikebe, Y., Ikeda, H., Inoue, H., et al. 1996, PASJ, 48, 157
Parmar, A. N., Guainazzi, M., Oosterbroek, T., Orr, A., Favata, F., Lumb, D., & Malizia, A. 1999, A&A, 345, 611
Perri, M., & Giommi, P. 2000, A&A, 362, L57
Piccinotti, G., Mushotzky, R. F., Boldt, E. A., Holt, S. S., Marshall, F. E., Serlemitsos, P. J., & Shafer, R. A. 1982, ApJ, 253, 485
Plionis, M., & Georgantopoulos, I. 1999, MNRAS, 306, 112
Protheroe, R. J., Wolfendale, A. W., & Wdowczyk, J. 1980, MNRAS, 192, 445
Risaliti, G., Maiolino, R., & Salvati, M. 1999, ApJ, 522, 157
Rosati, P., Tozzi, P., Giacconi, R., Gilli, R., Hasinger, G., Kewley, L., Mainieri, V., Nonino, M., et al. 2002, ApJ, 566, 667
Scharf, C. A., Jahoda, K., Treyer, M., Lahav, O., Boldt, E., & Piran, T. 2000, ApJ, 544, 49
Schmidt, M., Hasinger, G., Gunn, J., Schneider, D., Burg, R., Giacconi, R., Lehmann, I., MacKenty, J., et al. 1998, A&A, 329, 495
Serlemitsos, P. J., Jalota, L., Soong, Y., Kunieda, H., Tawara, Y., Tsusaka, Y., Suzuki, H., Sakima, Y., et al. 1995, PASJ, 47, 105
Shafer, R. A., & Fabian, A. C. 1983, in Early Evolution of the Universe and Its Present Structure, ed. G. O. Abell & G. Chincarini (Dordrecht: Reidel), 333
Shibata, R., Matsushita, K., Yamasaki, N. Y., Ohashi, T., Ishida, M., Kikuchi, K., Böhringer, H., & Matsumoto, H. 2001, ApJ, 549, 228
Snowden, S. L., Egger, R., Freyberg, M. J., McCammon, D., Plucinsky, P. P., Sanders, W. T., Schmitt, J. H. M. M., Trümper, J., & Voges, W. 1997, ApJ, 485, 125
Snowden, S. L., Freyberg, M. J., Plucinsky, P. P., Schmitt, J. H. M. M., Trümper, J., Voges, W., Edgar, R. J., McCammon, D., & Sanders, W. T. 1995, ApJ, 454, 643
Takahashi, T., Markevitch, M., Fukazawa, Y., Ikebe, Y., Ishisaki, Y., Kikuchi, K., Makishima, K., Tawara, Y., & ASCA Image analysis working group 1995, ASCA News, 3, 34, available on the WWW at ⟨http://heasarc.gsfc.nasa.gov/docs/asca/newsletters/ext_src_analysis3.html⟩
Tanaka, Y., & Bleeker, J. A. M. 1977, Space Sci. Rev., 20, 815
Tozzi, P., Rosati, P., Nonino, M., Bergeron, J., Borgani, S., Gilli, R., Gilmozzi, R., Hasinger, G., et al. 2001, ApJ, 562, 42
Tsusaka, Y., Suzuki, H., Yamashita, K., Kunieda, H., Tawara, Y., Ogasaka, Y., Uchibori, Y., Honda, H., et al. 1995, Appl. Opt., 34, 4848
Ueda, Y., Ishisaki, Y., Takahashi, T., Makishima, K., & Ohashi, T. 2001, ApJS, 133, 1
Ueda, Y., Takahashi, T., Inoue, H., Tsuru, T., Sakano, M., Ishisaki, Y., Ogasaka, Y., Makishima, K., Yamada, T., & Ohta, K. 1998, Nature, 391, 866
Ueda, Y., Takahashi, T., Inoue, H., Tsuru, T., Sakano, M., Ishisaki, Y., Ogasaka, Y., Makishima, K., et al. 1999a, ApJ, 518, 656
Ueda, Y., Takahashi, T., Ishisaki, Y., Ohashi, T., & Makishima, K. 1999b, ApJ, 524, L11
Vecchi, A., Molendi, S., Guainazzi, M., Fiore, F., & Parmar, A. N. 1999, A&A, 349, L73
Voges, W., Aschenbach, B., Boller, Th., Bräuninger, H., Briel, U., Burkert, W., Dennerl, K., Englhauser, J., et al. 1999, A&A, 349, 389, available on the WWW at ⟨http://rosat.gsfc.nasa.gov/docs/rosat/survey/rass-bsc/rass-bsc1-fmt.html⟩
Warwick, R. S., Pye, J. P., & Fabian, A. C. 1980, MNRAS, 190, 243
Wood, K. S., Meekins, J. F., Yentis, D. J., Smathers, H. W., McNutt, D. P., Bleach, R. D., Byram, E. T., Chubb, T. A., Friedman, H., & Meidav, M. 1984, ApJS, 56, 507